

On the Evolution of High-Redshift Active Galactic Nuclei

Jirong Mao^{1,2,3} and Minsun Kim³

jirongmao@mail.ynao.ac.cn

ABSTRACT

We build a simple physical model to study the high-redshift active galactic Nucleus (AGN) evolution within the co-evolution framework of central black holes (BHs) and their host galaxies. The correlation between the circular velocity of a dark halo V_c and the velocity dispersion of a galaxy σ is used to link the dark matter halo mass and BH mass. The dark matter halo mass function is converted to the BH mass function for any given redshift. The high-redshift optical AGN luminosity functions (LFs) are constructed. At $z \sim 4$, the flattening feature is not shown at the faint end of the optical AGN LF. This is consistent with observational results. If the optical AGN LF at $z \sim 6$ can be reproduced in the case in which central BHs have the Eddington-limited accretion, it is possible for the AGN lifetime to have a small value of 2×10^5 yrs. The X-ray AGN LFs and X-ray AGN number counts are also calculated at $2.0 < z < 5.0$ and $z > 3$, respectively, using the same parameters adopted in the calculation for the optical AGN LF at $z \sim 4$. It is estimated that about 30 AGNs per deg^2 at $z > 6$ can be detected with a flux limit of $3 \times 10^{-17} \text{ erg cm}^{-2} \text{ s}^{-1}$ in the $0.5 - 2 \text{ keV}$ band. Additionally, the cosmic reionization is also investigated. The ultraviolet photons emitted from the high-redshift AGNs mainly contribute to the cosmic reionization, and the central BHs of the high-redshift AGNs have a mass range of $10^6 - 10^8 M_\odot$. We also discuss some uncertainties in both the AGN LFs and AGN number counts originating from the $M_{\text{BH}} - \sigma$ relation, Eddington ratio, AGN lifetime, and X-ray attenuation in our model.

Subject headings: black hole physics — cosmology: theory — galaxies: active — galaxies: evolution — quasars: general — surveys

¹Yunnan Observatories, Chinese Academy of Sciences, 650011 Kunming, Yunnan Province, China

²Key Laboratory for the Structure and Evolution of Celestial Objects, Chinese Academy of Sciences, 650011 Kunming, China

³Korea Astronomy and Space Science Institute, 776, Daedeokdae-ro, Yuseong-gu, Daejeon 305-348, Republic of Korea

1. Introduction

Active galactic nucleus (AGN) evolution is one of the vital issues to investigate the central black hole (BH) accretion, galaxy formation, and large-scale structure of the universe. Some statistical results, such as luminosity functions (LFs) and number counts, can be obtained from multi-wavelength sky surveys. The optical LFs of quasi-stellar objects (QSOs) were obtained from the 2dF survey (Boyle et al. 2000; Croom et al. 2004). Using the data from ROSAT, *Chandra*, and XMM-*Newton* satellites, Miyaji et al. (2000), Miyaji et al. (2001), and Hasinger et al. (2005) constructed the soft X-ray AGN LFs in the 0.2 – 2 keV band. The hard X-ray LFs and hard X-ray cosmic background in the 2 – 10 keV band were studied as well (Cowie et al. 2003; Ueda et al. 2003; Barger et al. 2005; La Franca et al. 2005). From these early studies, we know that neither density evolution nor luminosity evolution can fully describe AGN LF evolutionary properties. However, a downsizing feature has been reported, which is the number density of galaxies/AGNs peaking at low redshift (Cowie et al. 1996; Lemaux et al. 2014; Ueda et al. 2014). Thus, the crucial explorations of the AGN LFs in the optical band for the high-redshift universe, which have been performed during recent years, have become more important. The QSO LFs at $3.6 < z < 5.0$ from the Sloan Digital Sky Survey (SDSS) have been given (Fan et al. 2001). The AGN LFs at $3.5 < z < 5.2$ have been extended to the faint end of $M_{1450} \sim -21.5$ by the great observatories origins deeps survey (GOODS) high-redshift AGN sample (Cristiani et al. 2004; Fontanot et al. 2007). The faint type-1 AGN LFs have been given by Bongiorno et al. (2007) from the VIMOS-VLT deep survey. With the 2dF-SDSS data, the AGN LF at $0.4 < z < 2.6$ has been extended 2.5 mag fainter (Croom et al. 2009) than the previous one. At $z \sim 4$, some faint end data points for QSO LF have been provided by the NOAO deep wide-field survey and the deep lens survey (Glikman et al. 2010). The AGN LFs at $z \sim 6$ were obtained by the SDSS deep survey (Jiang et al. 2009) and the Canada-France high-redshift QSO survey (Willott et al. 2010a). The Subaru high-redshift QSO survey has also discovered some faint AGNs at $z \sim 6$ (Kashikawa et al. 2014). High-redshift AGN detections in the X-ray band are also exciting. From the XMM-*Newton* medium-sensitivity survey, Ebrero et al. (2009) have derived AGN LFs ($0 < z < 3$) which can be described by a luminosity-dependent density evolution (LDDE) model. The AGN LF at $z \leq 5$ obtained from a faint *Chandra* sample has been reported by Yencho et al. (2009). Aird et al. (2010) have found the high space density of low-luminosity AGNs at $z > 2$ from the 2 Ms *Chandra* deep survey and the AEGIS-X 200 ks survey. The number counts of X-ray selected QSOs at $z > 3$ have been obtained from the COSMOS survey and the Subaru/XMM-*Newton* deep survey (Brusa et al. 2009; Civano et al. 2011; Hiroi et al. 2012). The number density evolution of obscured AGNs has been mentioned by Fiore et al. (2008, 2009), Brusa et al. (2010), and Hiroi et al. (2012). AGNs with column densities above 10^{24} cm^{-2} are denoted as “Compton thick”, and these

heavily obscured AGNs represent a key phase of AGN-host galaxy co-evolution. It is quite interesting that two Compton-thick AGNs have been discovered in the *XMM-Newton* deep survey ($z = 3.7$) and the 4 Ms *Chandra* deep field (CDF) survey ($z = 4.76$), respectively (Comastri et al. 2010a; Gilli et al. 2011). The Compton-thick AGN surveys have been done by Brightman et al. (2014) and Lanzuisi et al. (2014). The AGN number density and the cosmic X-ray background have been studied with large observational samples (Ueda et al. 2014; Aird et al. 2015; Miyaji et al. 2015).

Some problems with the AGN LF have been raised by these new observations. For example, at $z > 4$, a flattening feature at $M_{1450} > -23$ seen in the optical AGN LF (Fontanot et al. 2007) was explained by the physics of central BH growth and AGN/supernova feedback (Lapi et al. 2006; Fontanot et al. 2006). However, the number density of faint optical AGNs ($-23 < M_{1450} < -21$) reported by Glikman et al. (2010) is about 10 times larger than that of Fontanot et al. (2007). With additional spectral identifications, Glikman et al. (2011) rebuilt the AGN LF at $z = 4$. However, the number density of these faint AGNs is still two times that given by Fontanot et al. (2007). This observational discrepancy was also mentioned by Fiore (2010). One possible reason for this discrepancy is as follows (Glikman et al. 2010, 2011). Fontanot et al. (2007) used the QSO spectral template of Cristiani & Vio (1990), which empirically determines a distribution of continua blueward of $\text{Ly}\alpha$, and the power-law spectral template has a slope of 0.7; Glikman et al. (2010, 2011) had the QSO spectral library template modified by a composite using the Gaussian distribution of power-law continua, and a slope of 0.5 is given in the spectral template. If the sample selected by Glikman et al. (2011) has better completeness than that selected by Fontanot et al. (2007), the flattening feature given by Fontanot et al. (2007) would be significantly reduced. While Masters et al. (2012) built the optical LFs at $3 < z < 5$ from the COSMOS survey field. The space density of faint AGNs at $z \sim 4$ is lower than the result of Glikman et al. (2011) by a factor of $3 \sim 4$. They suggested that this discrepancy may be due to the contamination of dwarf stars and high- z galaxies in the sample of Glikman et al. (2011), and spectroscopic follow-up identification is still challenging for this contamination constraint. Therefore, the final high-redshift AGN candidates are different due to different selection functions. Although the AGN LF at $z \sim 6$ has been extended to the faint end of $M_{1450} \sim -22$, it seems that the AGN LF is still steep at the faint end (Willott et al. 2010a; Kashikawa et al. 2014).

One widely accepted issue of AGN evolution is that the AGN and its host galaxy have co-evolution characteristics (Richstone et al. 1998). A strong correlation was found between the central BH mass M_{BH} of a normal galaxy and the velocity dispersion σ of a galactic bulge (Ferrarese & Merritt 2000; Gebhardt et al. 2000; Tremaine et al. 2002; Gültekin et al. 2009; Batcheldor 2010). This $M_{\text{BH}} - \sigma$ relation (presented as $\log M_{\text{BH}} = \alpha + \beta \log(\sigma/200 \text{ km s}^{-1})$, where α and β are fitting parameters) is also valid for the AGN population (Shields et al.

2003, 2006; Greene & Ho 2007; Wu 2007; Woo et al. 2010). A correlation between a BH mass M_{BH} and the galactic spheroid mass M_{sph} (Magorrian et al. 1998; Marconi & Hunt 2003; Haring & Rix 2004; Nelson et al. 2004) also indicates the co-evolution feature of AGNs and their host galaxies. Moreover, the $M_{\text{BH}} - \sigma$ relation evolves with redshift, and the ratio between the M_{BH} and M_{sph} increases with redshift (Shields et al. 2006; McLure et al. 2006; Decarli et al. 2010). These evolution properties provide the possibility that the central BH growth could finish before its host spheroid formation. In other words, massive BHs grow rapidly in the early universe without commensurate growth of their host galaxies (Grupe & Mathur 2004; Shields et al. 2006). On the contrary, Schulze & Wisotzki (2014) performed a fitting procedure of the BH-bulge relation with the Monte Carlo simulation test, in which the observational selection effects were considered. They did not find any cosmological evolution of the BH-bulge relation when the selection effects were corrected. On the other hand, Loeb & Peebles (2003) suggested that the circular velocity V_c of a dark matter halo potential well can be linked to the velocity dispersion σ of a galactic bulge, and the theoretical relationship between σ and V_c was also examined by observational data (Ferrarese 2002). Therefore, we can link the physical processes of dark matter halos to those of baryons at a certain redshift.

Theoretical investigations of co-evolution have been carried out between central BHs and their host galaxies (Silk & Rees 1998; Fabian 1999; King 2003, 2005; Begelman & Nath 2005; Croton 2009; Nayakshin et al. 2009; King 2010). Shankar et al. (2009a) predicted the velocity dispersion functions of spheroid galaxies at $0 < z < 6$. Their results indicate a redshift evolution of the $M_{\text{BH}} - \sigma$ relation. Similar evidence for the evolution of the $M_{\text{BH}} - \sigma$ relation was given by numerical simulations (Robertson et al. 2006). The redshift evolution of a $M_{\text{BH}}/M_{\text{sph}}$ was also modeled (Somerville 2009; Lamastra et al. 2010). Haehnelt & Rees (1993) presented a QSO evolution model in which massive BHs are formed inside virialized dark matter halos. AGN LFs were studied within the framework of co-evolution between central BHs and their host galaxies, and the BH accretion history was explored in detail (Haehnelt et al. 1998). A linear relation between a dark matter halo mass and BH mass was used to derive the AGN LF (Haiman & Loeb 1998; Wyithe & Loeb 2002), and the processes of BH self-regulated growth were also considered (Wyithe & Loeb 2003). Several complicated models of QSO activity, including the BH accretion process (Mahmood et al. 2005) and the BH merger process (Shen 2009), were given as well. From numerical simulations, Hopkins et al. (2005) proposed a luminosity-dependent AGN lifetime to reproduce the AGN LFs. The AGN/supernova feedback processes were used to explain the observational down-sizing feature of the AGNs/BHs (Croton et al. 2006; Fontanot et al. 2006; Lapi et al. 2006, 2014; Marulli et al. 2008; Menci et al. 2008). Lapi et al. (2006) noticed that AGN shining occurs after dark matter halo virialization due to the growth of a central BH seed. Thus, a

time delay between dark matter halo virialization and AGN shining should be considered. In this case, super-Eddington accretion is important for the central BH growth.

Based on a semi-analytic model of the co-evolution between BHs and their hosts, Fanidakis et al. (2012) investigated the AGN evolution, considering both the thin-disk accretion and the ADAF model. The optical and X-ray AGN LFs were reproduced when the AGN obscuration form of Hasinger (2008) was taken into account. This model predicted a hierarchical buildup of BH mass, but the downsizing feature for different AGN populations was clearly shown due to the different accretion modes and the AGN obscuration. Hirschmann et al. (2012) comprehensively investigated some accretion modes. Standard accretion, varying sub-Eddington limit for the maximum accretion, and disk instability accretion were considered. The BH seed mass for the merger process was also considered. A cosmological numerical simulation for the BH growth was performed by Hirschmann et al. (2014). The downsizing feature of the AGN number density evolution was well explained when the gas density nearby the massive BH was included in their model. Thus, the processes of star formation and AGN/supernova feedback should be also involved. The star formation process was further explored by Enoki et al. (2014). In their semi-analytic model, the starburst is caused by an AGN merger, and the cold gas accretion triggers AGN shining. The amount of cold gas for the BH accretion decreases with cosmic time, and the AGN lifetime decreases with redshift. Then, the downsizing trend of the AGN evolution is shown. From above theoretical models, the observed downsizing feature of the AGN evolution can also be explained under the framework of the hierarchical structure formation.

Some research efforts have been attempted toward explaining the faint end of the high-redshift AGN LFs. Hopkins et al. (2007) determined the bolometric AGN LF at $0 < z < 6$ using a large set of AGN LFs in different rest-frame wavelengths. The faint-end slope of the AGN LF was confirmed. Shankar et al. (2009b, 2010, 2013) comprehensively studied bolometric LFs through the arrangements of BH accretion, radiative efficiency of AGNs, and AGN clustering. However, it was pointed out by Willott et al. (2010a) that those LFs built by Hopkins et al. (2007) and Shankar et al. (2009b) overestimated the number density of faint AGNs at $z = 6$. For instance, in a luminosity range of $-25.5 < M_{1450} < -24.5$, the AGN number density calculated by Shankar et al. (2009b) is about five times larger than those given by Jiang et al. (2009) and Willott et al. (2010b). Moreover, the predictions of high-redshift AGN number counts in the X-ray band are also uncertain. Rhoads & Haehnelt (2008) proposed a dark matter halo merger model to drive AGN shining. Marulli et al. (2008) constructed a semi-analytic model of the co-evolution between BHs and host galaxies. It was assumed that central BHs continuously accrete surrounding hot gas for AGN shining. As reported by Gilli et al. (2011), at $z > 6$, with a flux limit of 3×10^{-17} erg cm⁻² s⁻¹ in the 0.2–2 keV band, an optimistic detection of 500–600 AGNs per deg² and a pessimistic detection of

~ 16 AGNs per deg^2 were predicted by Rhook & Haehnelt (2008) and Marulli et al. (2008), respectively. Because many obscured low-luminosity AGNs can be found at high redshifts (La Franca et al. 2005; Hasinger 2008; Menci et al. 2008), high-redshift AGN detections in the X-ray band are strongly encouraged by some satellite proposals. For example, the Wide Field X-ray Telescope (WFXT) can perform deep observations in 100 deg^2 to a flux limit of $3 \times 10^{-17} \text{ erg cm}^{-2} \text{ s}^{-1}$ in the $0.5 - 2 \text{ keV}$ band (Rosati et al. 2010). Those unobscured AGNs beyond redshift 6 can be effectively detected. Some obscured AGNs can also be explored up to $z \sim 4$ (Comastri et al. 2010a; Gilli et al. 2011). Therefore, modeling predictions of the high-redshift AGN number density in the X-ray band could also be important for future missions.

The ultraviolet photons emitted by AGNs can effectively ionize the intergalactic medium (IGM). High-redshift AGN LFs are used to study cosmic reionization. The so-called Gunn-Peterson trough (Gunn & Peterson 1965) seen in the optical spectra of the SDSS AGN sample provides excellent evidences to constrain the cosmic reionization epoch (Fan et al. 2002, 2006a). It was estimated by Fan et al. (2006b) that the QSO contribution to the ionizing background is less than 30% of the star-forming galaxy contribution. The AGN contribution to the cosmic reionization (Shankar & Mathar 2007) was revisited by Glikman et al. (2010). However, the Subaru high-redshift quasar survey has shown that the AGNs at redshift 6 still do not have enough photons to ionize the universe (Kashikawa et al. 2014). In this paper, as a consequent issue of the high-redshift AGN evolution, some rough estimations for the cosmic reionization are given.

We build a simple analytic model to study high-redshift AGN evolution within the framework of joint evolution between central BHs and their host galaxies. Beginning from the dark matter halo mass function, we derive the AGN LFs by applying the $M_{\text{BH}} - \sigma$ and $V_c - \sigma$ relations. High-redshift AGN number counts in the X-ray band are obtained as well. We compare our results to those observational data. The cosmic reionization is also examined. In our physical recipe, the Eddington ratio λ , AGN lifetime τ_{AGN} , α , and β in the $M_{\text{BH}} - \sigma$ relation, are free parameters (see Table 1 for details). All of these parameters are within their observational constraints. We do not perform optimized fittings to those observational AGN LF data by adjusting the parameters in our model. Instead, we choose reasonable values for these parameters to produce the AGN LFs and AGN number counts by comparison with the observational data. Thus, some related physical processes can be further explored. Section 2.1 describes our physical model. The AGN LFs and AGN number counts are derived in Section 2.2. In Section 3, the contributions from the high-redshift AGNs to the cosmic reionization are estimated. Discussion and conclusions are given in Sections 4 and 5, respectively. Throughout the paper, we adopt the following cosmological parameters: $H_0 = 72 \text{ km s}^{-1} \text{ Mpc}^{-1}$, $\Omega_{\text{m}} = 0.3$, and $\Omega_{\Lambda} = 0.7$.

2. High-Redshift AGN Evolution

2.1. Model Description

AGN LF is one of the powerful tools to investigate central BH accretion and host galaxy evolution. Some examples of the AGN LF formulism have been derived (Wyithe & Loeb 2002, 2003; Lapi et al. 2006; Shen 2009). In this paper, we derive the AGN LF as follows:

$$\Phi(L, z) = \frac{dn_{\text{AGN}}}{d\log L} = \frac{d^2N}{dM_{\text{halo}}dz} \frac{dM_{\text{halo}}}{dM_{\text{BH}}} \frac{dM_{\text{BH}}}{d\log L} \frac{dz}{dt} \tau_{\text{AGN}}, \quad (1)$$

where M_{halo} is the mass of a dark matter halo, M_{BH} is the mass of a BH, L is the luminosity in a certain observational band, dN/dM_{halo} is the dark matter halo mass function. We further calculate the time derivative of dN/dM_{halo} (Sasaki 1994; Kitayama & Suto 1996). The result contains two terms, which are formation and destruction terms. Here, we only keep the formation term written as $d^2N/dM_{\text{halo}}dz$ and ignore the destruction term. Therefore, it is assumed that an AGN is formed inside a newly formed dark matter halo at a certain redshift, and the dark matter halo merger effect is not included in our model. We also assume that dark matter halos are virialized to harbor AGNs. The relation of M_{halo} and M_{BH} is given by $dM_{\text{halo}}/dM_{\text{BH}} = (dM_{\text{halo}}/dV_c)(dV_c/d\sigma)(d\sigma/dM_{\text{BH}})$, where V_c is the circular velocity of the dark matter halo potential well, and σ is the velocity dispersion of the host galaxy. The AGN lifetime τ_{AGN} is far less than the cosmic time. Therefore, to derive AGN LF, seven physical issues are involved in our procedure: the dark matter halo formation rate and the $M_{\text{halo}} - V_c$ relation are related to the dark matter halo mass function and the dark matter halo potential well, respectively; the $V_c - \sigma$ relation is applied to link the dark matter halo mass to the BH mass; the $M_{\text{BH}} - \sigma$ relation indicates the relation between the central BH and the host galaxy; the BH accretion is related to the physical properties of the central BH; the bolometric correction should be considered when we transfer bolometric luminosity to a specific luminosity in the optical/X-ray band; and the AGN lifetime is the AGN shining timescale in either the optical or X-ray band. In the following subsections, we describe these physical points adopted in our model in detail.

2.1.1. Link between Dark Matter Halos and BHs

The dark matter halo mass function dN/dM_{halo} at a certain redshift can be described by the Press-Schechter function (Press & Schechter 1974). Here, we use the dN/dM_{halo} form given by Sheth & Tormen (1999, 2002), which is more accurate than the Press-Schechter function at high-redshift (Springel et al. 2005). The dark matter halo formation rate $d^2N/dM_{\text{halo}}dz$ can also be calculated (Sasaki 1994; Kitayama & Suto 1996). The circular velocity of the

dark matter halo can be obtained as $V_c = 375(M_{\text{halo}}/10^{12} M_{\odot})^{1/3}((1+z)/7)^{1/2} \text{ km s}^{-1}$ (Loeb & Peebles 2003). With a certain density profile of the dark matter halo, Loeb & Peebles (2003) extrapolated V_c from the virial radius of a dark matter halo to the effective radius of a galaxy, and a factor of $1/\sqrt{2}$ was multiplied to this circular velocity at the effective radius. The final result was regarded as the line-of-sight velocity dispersion of the galaxy. We use their results and choose the Navarro-Frenk-White (NFW) density profile of the dark matter halo (Navarro et al. 1997). Thus, an approximation relation $\sigma = 0.69V_c$ is obtained. This theoretical result is consistent with the linear fit of $\sigma = (0.65 \pm 0.02)V_c$ from the observational data (Ferrarese 2002). Applying this theoretical $V_c - \sigma$ relation and the $M_{\text{BH}} - \sigma$ relation described in the next subsection, we can link the dark matter halo mass to the BH mass.

We use the $V_c - \sigma$ relation to link the BH mass and dark matter halo mass. However, some data points from the σ and V_c measurements of bulgeless galaxies (Kormendy & Bender 2011) have a strong deviation to the previous $V_c - \sigma$ relation given by Ferrarese (2002). Here, we mention that the BH mass considered in this paper is larger than $10^6 M_{\odot}$. Most bulgeless galaxies selected in the work of Kormendy & Bender (2011) have a velocity dispersion less than 60 km s^{-1} . This velocity dispersion put a constraint on the central BH mass, which is less than $10^6 M_{\odot}$. Therefore, these low-mass central BHs and related low-mass galaxies are not within our consideration of AGN LFs and AGN number counts. Moreover, Volonteri & Natarajan (2009b) found that low-mass bulgeless galaxies are unlikely to host central BHs. Furthermore, Volonteri et al. (2011) re-examined those observational data. They reported that the $M_{\text{BH}} - V_c$ correlation may be as strong as the $M_{\text{BH}} - \sigma$ relation. Thus, we think that the correlation between the central BH and dark matter halo is valid to derive the AGN LFs and AGN number counts at high redshifts. In the following subsections, we focus on the physical processes of both central BHs and their host galaxies, which are related to AGN LFs.

2.1.2. Co-evolution between BHs and Their Host Galaxies

Central BH accretion and AGN activity are strongly related to the AGN environment and host galaxy evolution (Silk & Rees 1998; Fabian 1999). Our AGN LF model is within the framework of co-evolution between AGNs and their host galaxies. Some important issues in our model are the $M_{\text{BH}} - \sigma$ relation, BH accretion, bolometric correction, and AGN lifetime. To derive the AGN LFs, the $M_{\text{BH}} - \sigma$ relation is required. This relation with a form of $M_{\text{BH}} \propto \sigma^5$ was first proposed by Silk & Rees (1998). It indicates a strong co-evolution between central BHs and their host galaxies. Because the AGN feedback has been considered, the form of $M_{\text{BH}} \propto \sigma^4$ can be derived (King 2003, 2005). In principle,

because the $M_{\text{BH}} - \sigma$ relation originates from a dynamic process, it should be independent of the observational wavelength. Robertson et al. (2006) examined the $M_{\text{BH}} - \sigma$ relation with the numerical simulation model. In their model, the circular velocity V_c is derived from the NFW dark matter halo profile. A certain gas fraction is given in each halo, and the BH seed grows through Bondi accretion. Especially, the feedback from both supernova and accreting BH is included. The final $M_{\text{BH}} - \sigma$ relation can be derived from a large set of hydrodynamic simulations with additional physics, such as the equation of state of the interstellar medium, galactic surface mass density, and dark matter concentration. Therefore, the $M_{\text{BH}} - \sigma$ relation of $\log M_{\text{BH}} = 8.01 + 4.02 \log(\sigma/200 \text{ km s}^{-1}) - 0.138 \log(1+z)$ computed by Robertson et al. (2006) is used in our model to reproduce the AGN LFs in the optical and X-ray bands. It is worth noting that this relation is dependent on the redshift. As mentioned in Section 1, the modeling results and the observational measurements for the $M_{\text{BH}} - \sigma$ relation are roughly consistent. However, the observational $M_{\text{BH}} - \sigma$ relation has an intrinsic scatter of 0.25 – 0.3 dex (Tremaine et al. 2002). Gültekin et al. (2009) investigated the intrinsic scatter of the $M_{\text{BH}} - \sigma$ relation in detail and re-examined the $M_{\text{BH}} - \sigma$ relation using updated data. As mentioned in their paper, there are systematic uncertainties when measuring the BH mass in a host galaxy. In this paper, we consider the effect of this intrinsic scatter in the $M_{\text{BH}} - \sigma$ relation. The best-fit of the $M_{\text{BH}} - \sigma$ relation from Gültekin et al. (2009) is $\log(M_{\text{BH}}/M_{\odot}) = (8.12 \pm 0.08) + (4.24 \pm 0.41) \log(\sigma/200 \text{ km s}^{-1})$. The intrinsic root-mean-square scatter of $\log(M_{\text{BH}}/M_{\odot})$ is given as 0.44 ± 0.06 , and this intrinsic scatter is assumed to be independent of σ . Taking into account the effect from this intrinsic scatter of the observational $M_{\text{BH}} - \sigma$ relation, we can reproduce the AGN LFs again. Thus, two kinds of AGN LFs, one derived by adopting a theoretical $M_{\text{BH}} - \sigma$ relation and the other by adopting an observational $M_{\text{BH}} - \sigma$ relation with an intrinsic scatter, are compared.

The accretion property of the central BH is a key point to produce the AGN bolometric luminosity. The Eddington ratio of accretion is defined by $\lambda = L_{\text{bol}}/L_{\text{edd}}$, where L_{bol} is the bolometric luminosity, and L_{edd} is the Eddington luminosity. The value of λ has a wide distribution with its peak range from 0.01 to 1 (Hopkins & Hernquist 2009; Shen 2009; Fanidakis et al. 2010). In the sub-Eddington accretion case of $\lambda \sim 0.5$, the bolometric AGN LF modeled by Shankar et al. (2009b) is about three to five times larger than observational ones at $z = 6$ within a luminosity range of $-25.5 < M_{1450} < -24.5$ (Willott et al. 2010a). While the Eddington ratio has been constrained as $\lambda \sim 1$ at $z = 6$ by the observations of Willott et al. (2010a) and Kashikawa et al. (2014). To investigate this problem, we try two accretion modes. We first adopt a sub-Eddington accretion of $\lambda = 0.25(M_{\text{BH}}/2 \times 10^9 M_{\odot})^{0.5}$ to reproduce the AGN LFs and AGN number counts in general. We also adopt a mode of $\lambda = 2.0(M_{\text{BH}}/2 \times 10^9 M_{\odot})^{0.5}$ to particularly reproduce the optical AGN LFs at $z \geq 6$. The accretion mode as a function of BH mass was proposed by Shankar et al. (2009b).

Although the low-mass BH growth at low redshift is suppressed with this accretion mode, the growth of high-mass BHs at high redshift can be well estimated. Shankar et al. (2009b) got somewhat better fits to the BH mass function in general with this accretion mode. From the observational point of view, most detected high-redshift AGNs have massive BHs with high accretion rates. In order to reproduce high-redshift AGN LFs, we focus on high-mass BHs with high accretion ratios. Thus, this accretion mode is adopted in our task. In Section 4, we further provide observational constraints and physical explanations on the accretion modes adopted in this work.

We perform the bolometric corrections, $k_B = L_{bol}/L_B$ and $k_x = L_{bol}/L_x$, to convert the bolometric luminosity L_{bol} to the B-band luminosity L_B and the X-ray luminosity L_x , respectively. Elvis et al. (1994) determined two observational values, $k_B = 11.4$ and $k_x = 35$, for broad-line AGNs. $k_x = 85$ was determined in the case in which AGNs have no broad-line feature (Barger et al. 2005). Here, we take the bolometric correction results of Marconi et al. (2004): $\log[L/L_x(2-10 \text{ keV})] = 1.54 + 0.24(\log L - 12) + 0.012(\log L - 12)^2 - 0.0015(\log L - 12)^3$, $\log[L/L_x(0.5-2 \text{ keV})] = 1.65 + 0.22(\log L - 12) + 0.012(\log L - 12)^2 - 0.0015(\log L - 12)^3$, and $\log(L/L_B) = 0.80 - 0.067(\log L - 12) + 0.017(\log L - 12)^2 - 0.0023(\log L - 12)^3$, where L is the bolometric luminosity in units of L_\odot . The template spectrum of Marconi et al. (2004) constructed by the intrinsic AGN spectral energy distribution (SED) enables us to precisely determine the AGN luminosities in different energy bands.

The AGN e-folding time given by the Salpeter timescale (Salpeter 1964; Marconi et al. 2004) is usually considered as the AGN lifetime. From AGN clustering measurements, we can obtain the AGN lifetime with a wide range from 10^6 to 10^8 years (Haiman & Hui 2001; Martini & Weinberg 2001). Haiman & Cen (2002) took the value of $\tau_{\text{AGN}} \sim 10^7$ yrs as the AGN lifetime for high-redshift QSOs. In the AGN-host galaxy joint evolution framework, we suggest different AGN lifetimes for different observational energy bands. At the initial coevolutionary stage of the central BHs and their host galaxies, AGN X-ray emission can be detected, but AGN optical emission is still fully absorbed. At a later stage, the AGN can be observed in the optical band when the AGN surrounding medium is transparent. Thus, the lifetime of the X-ray selected AGNs could be longer than that of the optically selected AGNs. Here, we take 2×10^7 and 9×10^7 years as reference values for the AGN lifetime to calculate the optical and X-ray AGN LFs, respectively. We take an exceptional case, in which the AGN lifetime is given as 2×10^5 yrs, to reproduce the optical AGN LFs at $z \geq 6$.

2.2. LFs and Number Counts

Assuming a sub-Eddington accretion of $\lambda = 0.25(M_{\text{BH}}/2 \times 10^9 M_{\odot})^{0.5}$, we use the $M_{\text{halo}} - V_c$, $V_c - \sigma$, and $M_{\text{BH}} - \sigma$ relations to derive the AGN LFs. As mentioned in Section 2.1, these relations adopted in our calculations are obtained from theoretical works. The AGN LFs derived from an observational $M_{\text{BH}} - \sigma$ relation are also given in this paper, and those effects from the intrinsic scatter of the observational $M_{\text{BH}} - \sigma$ relation are investigated. Below, we present our results in detail.

2.2.1. AGN LFs in the Optical and X-Ray Bands

We show the optical AGN LFs at $z = 4$ in Figure 1. The deep GOODS observation with a sky area of 320 arcmin^2 provides a faint ($M_{1450} \leq -21$) AGN sample (Fontanot et al. 2007). The AGN LF from the NOAO Deep Wide-Field Survey and the Deep Lens Survey with a total area of 3.76 deg^2 (Glikman et al. 2010) is also shown. We clearly see that the AGN LF from these GOODS data has lower values than the AGN LF from Glikman et al. (2010) at $M_{1450} > -23$. With a sub-Eddington accretion of $\lambda = 0.25(M_{\text{BH}}/2 \times 10^9 M_{\odot})^{0.5}$ and an AGN lifetime of 2×10^7 yrs, we calculate the optical AGN LF at $z = 4$, and our result is consistent with that of Glikman et al. (2010). As we described in Section 1, the discrepancies shown among the LFs of Glikman et al. (2010, 2011), Fontanot et al. (2007), and Masters et al. (2012) could be due to the different selection functions used to select high-redshift AGN candidates. The spectral identification is challenging to identify faint AGNs at high redshift. Moreover, at present, large error bars are given at the faint end of both LFs from Glikman et al. (2010) and Fontanot et al. (2007). Thus, the discrepancy has large uncertainty.

We show the optical AGN LFs at $z = 6$ in Figure 2. Six QSOs down to a magnitude of $M_{1450} \sim -25$ were found from the SDSS deep stripe (Jiang et al. 2009). The result from the Canada-France high- z quasar survey (Willott et al. 2010b) is also shown. The data point at the faintest magnitude of $M_{1450} \sim -22.2$ was estimated by the single quasar from the Subaru/XMM-*Newton* Deep Survey. Data points from the Subaru high-redshift quasar survey (Kashikawa et al. 2014) are also shown. With the same physical parameters used to reproduce the AGN LF at $z = 4$, we compute the AGN LFs at $z = 6$, and the results are shown in Figure 2. In addition, our predictions for the optical AGN LFs at $z = 8$ and $z = 9.5$ are shown in Figure 3.

The AGN LFs estimated by our model are roughly consistent with those from updated observational data at $z = 4$. At $z = 6$, our results seem to be consistent with the observa-

tional data given by Jiang et al. (2009) in a luminosity range of $-28 < M_{1450} < -24$. In general, we do not have the overestimation problems that were mentioned by Hopkins et al. (2007) and Shankar et al. (2009b). However, our AGN LF at the faint end of $M_{1450} = -22.2$ is 10 times larger than the observational one. We note that only a single quasar was used to build that data point (Willott et al. 2010a,b). Therefore, at $z = 6$, the observational AGN LF at the faint end is still poorly constrained, although the observational AGN LF still seems steep at the faint end when we consider the data points of the Subaru high-redshift quasar survey (Kashikawa et al. 2014). From our results, we expect that more faint AGNs can be detected by some wide-field surveys of the Subaru telescope, such as the Hyper Suprime-Cam (HSC) survey and the Prime Focus Spectrograph (PFS) survey, in the future.

The AGNs at $z = 6$ have been identified by Willott et al. (2010a,b) and Kashikawa et al. (2014), and the central BHs with a mass of $10^8 M_{\odot}$ have Eddington-limited accretion. Therefore, we take the accretion mode of $\lambda = 2.0(M_{\text{BH}}/2 \times 10^9 M_{\odot})^{0.5}$ and reproduce the optical AGN LF at $z \sim 6$. The results are shown in Figures 2 and 3. With this accretion mode, it is possible to take an AGN lifetime of 2×10^5 yrs so that our results are roughly consistent with the observational data of Willott et al. (2010b) and Kashikawa et al. (2014). This indicates that those AGNs at $z = 6$ detected by Willott et al. (2010b) and Kashikawa et al. (2014) may be very young.

We also predict optical AGN LFs at $z = 8$ and $z = 9.5$ shown in Figure 3. Two parameter sets, one set for the sub-Eddington accretion of $\lambda = 0.25(M_{\text{BH}}/2 \times 10^9 M_{\odot})^{0.5}$ and an AGN lifetime of 2.0×10^7 yrs, and the other set for the Eddington accretion of $\lambda = 2.0(M_{\text{BH}}/2 \times 10^9 M_{\odot})^{0.5}$ and an AGN lifetime of 2.0×10^5 yrs, are adopted in our prediction. The $M_{\text{BH}} - \sigma$ relation of Robertson et al. (2006) is used in the above calculations. These estimated results can be constrained by future optical observations and surveys as well.

Two kinds of AGN LFs, one derived with the theoretical $M_{\text{BH}} - \sigma$ relation (Robertson et al. 2006) and the other with the observational $M_{\text{BH}} - \sigma$ relation (Gültekin et al. 2009), are given in this paper. We put lower and upper limits on our AGN LFs by considering the intrinsic scatter of the observational $M_{\text{BH}} - \sigma$ relation. We can distinguish different AGN LFs shown in Figures 1 and 2. Although our AGN LFs derived from the theoretical $M_{\text{BH}} - \sigma$ relation are in good agreement with those derived from the observational $M_{\text{BH}} - \sigma$ relation, we clearly see that the AGN LFs at high redshifts have uncertainties.

Both type-1 (broad-line) and type-2 (narrow-line) AGNs are included in the calculation of the optical AGN LFs. The observational sample adopted in this paper contains only type-1 AGNs. In principle, with X-ray telescopes, type-1 AGNs are detected as unobscured AGNs, and most type-2 AGNs can be effectively detected as obscured AGNs (Risaliti et al. 1999). However, X-ray-selected AGNs and optical-selected AGNs have different classifications (Gilli

et al. 2001; Matt 2002). Because we have neither a one-to-one correspondence between type-1 and unobscured AGNs, nor that between type-2 and obscured AGNs, it is difficult to know the fraction of type-1 AGNs and type-2 AGNs in the optical band at high redshifts (Mayo & Lawrence 2013). Although the number density of obscured AGNs is four times larger than that of unobscured AGNs (Risaliti et al. 1999), low-luminosity AGNs are more frequently obscured than high-luminosity AGNs (Lawrence 1991; Ueda et al. 2003).

We obtain the AGN LFs in the 2 – 10 keV band using the $M_{\text{BH}} - \sigma$ relations of Robertson et al. (2006) and Gültekin et al. (2009). The AGN LFs at $z = 2.25$, $z = 3.0$, and $z = 4.5$ are shown in Figures 4-6, respectively. A sub-Eddington accretion of $\lambda = 0.25(M_{\text{BH}}/2 \times 10^9 M_{\odot})^{0.5}$ and an AGN lifetime of 9×10^7 yrs are adopted in these calculations. For comparison, we show the observational data from the CDF and the all-wavelength extended growth strip international survey (AEGIS) in the redshift ranges of $2.0 < z < 2.5$ and $2.5 < z < 3.5$ (Aird et al. 2010). In the work of Aird et al. (2010), the spectral identification and the color pre-selected identification were used for AGN selection. In particular, the color pre-selected processes are as follows. AGN candidates are first selected by the Lyman-break technique (Steidel et al. 2003) from the optical deep surveys based on their optical colors. Then these color pre-selected objects are matched by X-ray point sources. Our results show general agreement with the observed data. In Figure 6, the AGN LF at $4.0 < z < 5.0$ given by Ueda et al. (2014) is also shown. At the faint end, our results have excess compared to the observational data, but the overall trend agrees with most observational data points.

Figure 7 shows our AGN LFs at redshifts 4.5, 5, and 6, respectively. The $M_{\text{BH}} - \sigma$ relation of Robertson et al. (2006) is adopted to reproduce these AGN LFs. The observational AGN LF at $4.0 < z < 5.0$ (Ueda et al. 2014) is also shown. We see that the number of luminous AGNs decreases with increasing redshift in our model. In contrast, at the low-luminosity part, the AGN LFs do not show any flattening evidence. These results are consistent with the trends for the observational AGN LFs given by Aird et al. (2010). Although the hierarchical structure formation feature is shown in the X-ray AGN LFs at $z > 3$, large X-ray data samples are required to further identify the AGN evolution properties at high redshifts.

2.2.2. High-redshift AGN Number Counts in the X-Ray Band

Some investigations of high-redshift AGN number counts in the X-ray band are also important. We follow the formalism of the cumulative number counts given by Ballantyne et al.

(2006) as follows:

$$N(> F) = \frac{K_{sr}c}{H_0} \int_{z_{min}}^{z_{max}} \int_{\max(\log L_{min}, \log L_F)}^{\log L_{max}} \Phi(L_x, z) \times \frac{d_l^2}{(1+z)^2 [\Omega_m(1+z)^3 + \Omega_\Lambda]^{1/2}} d\log L_x dz, \quad (2)$$

where $\Phi(L_x, z)$ is the X-ray AGN LF, $K_{sr} = 3 \times 10^{-4}$ is the conversion factor from sr^{-1} to deg^{-2} , L_F is the rest-frame luminosity corresponding to the observed-frame flux F at redshift z , d_l is the luminosity distance, $\log L_{min} = 41.5$ and $\log L_{max} = 48$.

We take the observational AGN number counts given by both Brusa et al. (2009) from the XMM-COSMOS survey and Civano et al. (2011) from the *Chandra*-COSMOS sample to compare with our results. AGN candidates from the XMM-COSMOS survey have spectral identifications in the optical band, and optical broad-lines are shown in the optical spectrum of each AGN. Half of the AGN sources in the *Chandra*-COSMOS sample also have optical broad-lines shown in their optical spectra. Therefore, we treat these X-ray selected AGNs as unobscured sources. However, Equation (2) contains contributions from both unobscured and obscured AGNs.

To specify the contribution of the unobscured/obscured AGNs to the AGN number counts in the X-ray band so that we can compare our results with those of the observational data, we use the statistical results given by Hasinger (2008). In that work, the obscured AGN fraction decreases with the X-ray luminosity but increases with redshift as $f = -0.226 \log L_x + 10.306$ and $f = 0.308(1+z)^{0.48}$, where f is the obscured AGN fraction. In this subsection, it is essential that we apply the intrinsically absorbed X-ray spectrum to obtain the observational X-ray flux. Then, we can derive the AGN number counts in the X-ray band. Given a certain intrinsic absorption N_H value, the X-ray spectral template can be confirmed. In Appendix A, we put some examples of intrinsically absorbed X-ray spectra at high redshifts. Finally, we can obtain high-redshift AGN number counts in the X-ray band with certain N_H values. Here, we notice one difference between the obscuration mentioned in this subsection and the attenuation from the AGN host galaxy. Based on the AGN unified model (Antonucci 2003), the classification of unobscured/obscured AGNs can be defined through X-ray spectra and X-ray hardness ratios. The attenuation property is decided by the AGN torus with different view angles, while the attenuation of an AGN host galaxy is identified as the absorption caused by dusty gas surrounding the central BH. However, the dusty gas is also the material for both central BH growth/accretion and star formation. We also note that Hopkins et al. (2011) combined two attenuation origins as one effect from the AGN torus.

We show the AGN number counts in the 0.5 – 2 keV band at $z > 3$ and $z > 4$ in Figures 8 and 9, respectively. The AGN number counts with different absorption N_H values ($1.0 \times 10^{22} \text{ cm}^{-2}$, $5.0 \times 10^{22} \text{ cm}^{-2}$, and $1.0 \times 10^{23} \text{ cm}^{-2}$) are given in each figure. The

theoretical $M_{\text{BH}} - \sigma$ relation (Robertson et al. 2006) is considered. Although our results of the X-ray AGN number counts are consistent with the observational data in general, the uncertainties of these results from the X-ray intrinsic attenuation are clearly shown.

We show the AGN number counts in the 0.5 – 2 keV band at $z > 4$, $z > 5$, and $z > 6$, respectively, in Figure 10. Our results derived from the $M_{\text{BH}} - \sigma$ relation of Robertson et al. (2006) are shown. The absorption N_{H} is fixed as $5.0 \times 10^{22} \text{ cm}^{-2}$. We also show the observational AGN number counts at $z > 4$ given by Brusa et al. (2009) and Civano et al. (2011) in Figure 10. Gilli et al. (2011) discovered one Compton-thick AGN at redshift 4.76 in the 4 Ms CDF-S field. This finding provides some observational evidences of the AGN attenuation properties: a hardness ratio of 0.23 and an intrinsic column density of 10^{24} cm^{-2} indicating a heavy absorption in the X-ray band, and a multi-wavelength SED fitting suggesting a strong star formation process. Compton-thick AGN surveys have recently been performed (Brightman et al. 2014; Lanzuisi et al. 2014). We hope that our results for the high-redshift AGN population can be constrained by all kinds of updated X-ray detections.

3. Simple Estimation of the AGN Contribution to Cosmic Reionization

The cosmic reionization epochs at redshift 6 and redshift 10.9 were constrained by the Gunn-Peterson trough (Gunn & Peterson 1965) of the high-redshift quasar spectra (Fan et al. 2002, 2006a) and the cosmic microwave background polarization of the Wilkinson Microwave Anisotropy Probe (*WMAP*) measurements (Spergel et al. 2006), respectively. Two fundamental points are involved in the topic of the cosmic reionization: (1) what kind of object can emit ionizing photons for the cosmic reionization and (2) how many ionizing photons can be emitted by these objects? It was suggested that some ionizing photons emitted from high-redshift AGNs can survive after attenuation by the surrounding medium; then, these photons can ionize the IGM (Madau et al. 1999). In this section, we estimate the contribution of high-redshift AGNs to the cosmic reionization.

We have calculated the optical AGN LFs at high redshifts in Section 2.2. Thus, we can sum up AGN emissions at a certain redshift and obtain the total ionization rate as $\dot{N}_{\text{ion}} = \int L\Phi(L, z)/(h\nu)dL$, where h is the Planck constant, and ν is the average ionizing frequency (Choudhury & Ferrara 2005).

To quantify the cosmic reionizing process of neutral hydrogen, the time evolution of the filling factor Q_{HII} has been derived by Shapiro & Giroux (1987) as follows:

$$\frac{dQ_{\text{HII}}}{dt} = \frac{\dot{N}_{\text{ion}}}{n_{\text{H}}} - \frac{Q_{\text{HII}}}{t_{\text{rec}}}, \quad (3)$$

where $n_{\text{H}} = 1.7 \times 10^{-7} \text{ cm}^{-3}$ is the number density of neutral hydrogen in the local universe, $t_{\text{rec}} = 0.3((1+z)/4)^{-3}(C/30)^{-1} \text{ Gyr}$ is the recombination time, and C is the clumping factor. Different solutions for Equation (3) were fully discussed by Meiksin (2005). $Q_{\text{HII}} \geq 1$ indicates the fully ionized case of the cosmic reionization, and the corresponding redshift is the reionization epoch. The clumping factor $C(z) = 17.6e^{-0.1z+0.0011z^2}$ was reported by Ilev et al. (2006). In the relevant reionization redshift interval of $7 < z < 10$, we obtain $7 < C < 10$. Here we adopt $C = 7$ as a reference value (Kaurov & Gnedin 2014). The photon number contributed to the cosmic reionization N_{ion} is multiplied by an escape fraction f_{esc} , because a part of photons emitted from AGNs are absorbed by the surrounding medium of AGNs and the AGN host galaxies. It is quite complicated to determine the value of the escape fraction f_{esc} . A brief discussion was given by Barton et al. (2004). It was pointed out that this parameter is dependent on star formation processes and dust production in primordial galaxies (Mao et al. 2007). Here, we take $f_{\text{esc}} = 0.5$ as a reference value.

We obtain different evolution traces for the filling factor. The results are shown in Figure 11. AGNs with a BH mass range of $1.0 \times 10^6 - 1.0 \times 10^7 M_{\odot}$ can reionize the Universe at $z \sim 8$, while AGNs with a BH mass range of $1.0 \times 10^7 - 1.0 \times 10^8 M_{\odot}$ can also reionize the Universe at $z \sim 7$. However, AGNs with a BH mass range of $1.0 \times 10^8 - 1.0 \times 10^9 M_{\odot}$ cannot fully reionize the Universe at $z > 6$. Therefore, we conclude that low-luminosity AGNs dominate the cosmic reionization. Recently, Bouwens et al. (2015) estimated some cosmic reionization processes. Using the SDSS AGN LF at $z = 5$ given by McGreer et al. (2013), they built luminosity evolution and density evolution models. They claimed that AGNs do not have enough photons for the cosmic reionization at $z > 6$. However, Giallongo et al. (2015) analyzed the AGN ionization emissivity at $z > 4$. Some faint AGN candidates at $z = 4 - 6.5$ have been detected from the GOODS observation, and optical AGN LFs have been derived. It has been suggested that the AGN population provides an important contribution to the cosmic reionization. From a theoretical point of view, Volonteri & Gnedin (2009) presented a simple high-redshift BH growth model. They also noted the importance of the AGN population for the cosmic reionization. Recently, Hao et al. (2015) proposed that intermediate BHs (mass range of $10^2 - 10^5 M_{\odot}$) shining at high redshifts emit UV photons to ionize the Universe. In our model, we predict the optical AGN LFs at $z = 6$. We estimate that photons from high-redshift AGNs can effectively ionize the universe at $z > 6$. However, at $z = 6$, the optical LF at the faint end in our model is 10 times that of the observational one. We expect that more faint AGNs at $z > 6$ can be detected in the future.

Although high-redshift AGNs seem to provide enough photons to fully reionize the Universe beyond redshift 6, the following considerations should be taken into account. First, those optical AGN LFs shown in Figure 2 have large uncertainties at the faint end. In particular, at a magnitude of $M_{1450} = -22.2$, our AGN LF at $z = 6$ is 10 times larger

than the observational one. Second, the determined reionization epochs in Figure 11 are dependent on the clumping factor C . Finally, the escape fraction f_{esc} value is referenced from the environment of young galaxies at high redshifts. We assume that the escape fraction of AGNs is the same as that of high-redshift galaxies. In summary, we expect that more faint AGNs beyond redshift 6 can be identified in the future if the cosmic reionization can indeed be dominated by the AGN activity.

Some of the primeval galaxies at redshift 6 – 10 detected from optical deep surveys are also candidates to fully reionize the Universe (Bouwens et al. 2006; Bunker et al. 2010; Robertson et al. 2010; Bouwens et al. 2011). Some reionization processes have been fully discussed (Dijkstra et al. 2007; Mao et al. 2007; Salvaterra et al. 2011). It is known that different kinds of objects are involved in cosmic reionization processes. Within the framework of joint evolution between central BHs and their host galaxies, we suggest two reionization stages. Ionizing photons emitted from proto-galaxies dominate the first stage of the cosmic reionization. In this stage, central BHs with masses less than $10^6 M_{\odot}$ are hidden inside proto-galaxies and ionizing photons are fully absorbed by the surrounding medium. After sufficient central BH growth and star formation, central BHs shine as typical AGNs, and the AGN environment is transparent. Ionizing photons emitted from AGNs may dominate the second stage of the cosmic reionization.

4. Discussion

4.1. “Flicker” Accretion

Accretion is one of the key points for AGN shining. As mentioned in Section 1, with the sub-Eddington accretion of $\lambda \sim 0.5$, Shankar et al. (2009b) overestimated the number density of faint AGNs in the luminosity range of $-25.5 < M_{1450} < -24.5$ at $z = 6$. We know that the QSOs at $z = 6$ found by Willott et al. (2010a,b) and Kashikawa et al. (2014) have an Eddington ratio close to the Eddington limit. In this paper, if we increase the Eddington ratio to the Eddington limit and decrease the AGN lifetime to 2×10^5 yrs, we can reproduce the optical AGN LF at $z = 6$. This indicates that BHs with a mass of $10^8 M_{\odot}$ accreting in the Eddington limit at $z = 6$ can form very young QSOs. Although we use a single Eddington ratio per BH mass, we realize that the accretion history during BH growth is related to the Eddington ratio (Granato et al. 2004). Shen (2009) investigated the BH growth in detail taking into consideration the evolution of the Eddington ratio. Aird et al. (2012) reported an observational distribution of the Eddington ratio, which is an universal function with a power-law shape. Thus, rather than a single Eddington ratio per BH mass, the Eddington ratio distribution should be taken into account when modeling the AGN LFs.

In our model, we use the single Eddington ratio form without any distribution function. We ignore complicated BH accretion processes during BH growth, and we think that the single Eddington accretion mode corresponds to the peak of the AGN lightcurve. Furthermore, because we find the AGN “flicker” phase at high redshift, it is reasonable that the peak of the AGN light curve occurs over the time of the AGN flicker phase. This peak/“flicker” time is much shorter than the averaged AGN lifetime. Therefore, the single accretion mode without any distribution scatter is helpful to explore the AGN short-time variability/burst given by Novak et al. (2011) and Schawinski et al. (2015).

4.2. AGN Lifetime

We propose a possible lifetime of 2.0×10^5 yrs for the optical AGNs at $z \geq 6$, and these high-redshift optical AGNs are younger than those in previous studies. For example, Bolton et al. (2011) provided the observational AGN bright phase at $z > 6$, and the AGN lifetime was constrained as $1.0 \times 10^6 - 1.0 \times 10^7$ yrs. Here, we further summarize some physical possibilities regarding on the AGN lifetime. There have been more high-redshift ($z \geq 6$) AGN findings (Reed et al. 2015; Venemans et al. 2015; Wu et al. 2015). If we use the BH growth scenario to explain massive AGNs at high-redshift, we expect massive AGN activity within the timescale of $1.0 \times 10^7 - 1.0 \times 10^8$ yrs. The AGN e-folding time and duty circle should be considered in the cosmological evolution scenario. However, it is still possible to have short-timescale variabilities in the AGN luminosity during the BH growth phase. This possibility could particularly be important for the study of high-redshift AGNs. Novak et al. (2011) performed two-dimensional simulations to study the time-dependence of BH accretion, and the AGN light curve within an AGN phase of 250 Myr can be divided by many short bursts with a typical timescale of 1.0×10^5 yrs. Gas supply for BH growth can be through instability-driven inflows (Bournaud et al. 2011). If BH growth occurs in a star-forming disk galaxy, BH accretion with short-time variability has been identified in numerical simulations (Gabor & Bournaud, 2013). Hickox et al. (2014) studied the connection between the BH activity and the star formation. They proposed that the timescale of 100 Myr corresponds to an average number of the whole BH accretion, while instantaneous luminosity corresponds to a variability with a much shorter timescale. Very recently, Schawinski et al. (2015) observationally defined the AGN lifetime, which is the ratio between the time to photoionize a host galaxy and the fraction of optically elusive AGNs. Due to the arguments on the switch-on (high-accretion rate) and switch-off (low-accretion rate) processes, Schawinski et al. (2015) claimed that the AGN “flicker” duration is 1.0×10^5 yrs based on the *Swift*-BAT and SDSS samples. We think that their results can support an AGN lifetime number on the order of 10^5 years adopted in our model for those Eddington-limited AGNs at $z \geq 6$.

In our model, the AGN lifetimes at different redshifts have different numbers. The AGN lifetime of 2.0×10^7 yrs is used in our model to reproduce the AGN LF at $z = 4$. If we take the “flicker” scenario given by Schawinski et al. (2015), we think that the AGN lifetime with an order of 10^7 yrs indicates an averaged AGN activity process with sub-Eddington accretion. At $z \geq 6$, we do not have enough observational data, and the observational AGN LF spreads in a relatively small range of luminosity. If we reproduce the optical AGN LF using the Eddington-limited accretion at $z \geq 6$, the “flicker” AGN lifetime of 2.0×10^5 yrs in the BH growth scenario can be understood as the time of the instantaneous AGN activity. We also speculate (1) there are enough gas clumps surrounding the central BH to fuel AGN shining at high redshift, so that the accretion rate is high, and we could identify violent short-time bursts of AGNs, and (2) at low-redshift, there are fewer gas clumps surrounding the central BH, so that the accretion rate is low, and we observe many AGNs without any violent short-time bursts. Thus, we emphasize that the general AGN lifetime is much longer than the lifetime of short-time bursts.

4.3. Feedback Effects

The AGN/supernova kinetic feedback effects are strongly involved in the galaxy formation and evolution: (1) heating the surrounding gas of a central BH and quenching the star formation of a galaxy bulge and (2) blowing away the surrounding gas of a central BH and stopping further BH growth. In particular, we note that the AGN feedback dominates in massive dark matter halos while the supernova feedback is effective in small dark matter halos (Granato et al. 2004). We further discuss the feedback effect of supernovae on the faint end of the AGN LF mentioned by Lapi et al. (2006) and Fontanot et al. (2007): a small dark matter halo potential well is not deep enough to contain cooling baryons if we consider supernova feedback, and further BH growth is not expected. Hence, there are no more low-mass BHs in small dark matter halos, and AGN LFs show a flattening feature at the faint end. However, this reasonable explanation is challenged by the optical AGN LF at $z \sim 4$ (Glikman et al. 2010). The AGN LF given by Glikman et al. (2010) does not show the flattening feature, indicating more faint AGNs in the high-redshift universe¹. Although it is likely that the supernova feedback effect on AGN LFs reported by Lapi et al. (2006) and Fontanot et al. (2007) is overestimated, we note that Masters et al. (2012) also presented the flattening feature at the faint end of the AGN LF. Moreover, strong supernova feedback can blow away the material surrounding a central BH, while the material surrounding a central

¹A shallow slope of the optical LF at $z \sim 4$ was reported by Ikeda et al. (2011). However, we note that the measurement of Glikman et al. (2010) is 2-3 mag deeper than that of Ikeda et al. (2011).

BH may exist when the supernova feedback is weak. Thus, weak supernova feedback can also be one possible reason that low-luminosity AGNs harbored in small dark matter halos suffer strong attenuation. In order to obtain quantitative results, some star formation and evolution processes, including the initial mass function and the star formation rate, should be explored in the future.

4.4. BH Merger Rates

Although we assume that BH accretion dominates the AGN evolution process, BH merger effects should be estimated. We assume that one BH is inside one dark matter halo, and the dark matter halo merger is followed by the central BH merger. Then, we can apply a simple treatment reported by Shankar et al. (2009b). The fraction of the BH merger is given as $F = P_{merg}\Delta t/t_H(z)$, where P_{merg} is the probability of the BH merging with equal-mass BH, $t_H(z)$ is the Hubble time, and Δt is the dark matter halo merging timescale. We assume $P_{merg} = 0.5$. From an investigation of the BH/dark matter halo merger (Kulkarni & Loeb 2011), we can obtain the value of $\Delta t/t_H(z)$. The variation of the BH mass function is $\Delta\Phi = F \times \Phi(M_{BH}/2)/2 - F \times \Phi(M_{BH})$. Finally, we obtain the BH merger effect on AGN LFs. As an example, in the case in which the dark matter halo has a mass of $1.0 \times 10^{12} M_\odot$, the BH merger effect provides variations of 17% and 15% on the AGN LFs at $z = 4$ and $z = 6$, respectively. Moreover, the variation of BH accretion caused by the BH merger can be ignored (Shankar et al. 2010). Besides these simple estimations mentioned above, in the following, we discuss some complicated issues. The so-called “dry merger”, which refers to the dark matter halo merger without baryons, has been put forward (van Dokkum et al. 2005). In this case, BHs do not merge even if dark matter halos have merging processes. This is one reason that not all of the major mergers end up with massive early-type galaxies (Chou et al. 2011). On the other hand, the dark matter halo merging timescale and the incoming BH merging timescale were studied by Shen (2009) and Kulkarni & Loeb (2011). At high-redshift, BHs sink to the center of the merged dark matter halo before BH merging. Therefore, at high redshift, binary BHs or triple BHs can stay in the same host galaxy. Thus, the $M_{BH} - \sigma$ relation should be revisited. These interesting topics are the next step in the future research.

4.5. High-redshift AGN Number Counts

The predictions of high-redshift AGN detection are helpful for future X-ray mission proposals. The WFXTE deep survey can cover an observational area of 100 deg^2 (Rosati et

al. 2010). In our model, to the flux limit of 3×10^{-17} erg cm $^{-2}$ s $^{-1}$ in the 0.5–2 keV band, we predict that ~ 30 AGNs per deg 2 with the absorption of $N_{\text{H}} = 5.0 \times 10^{22}$ cm $^{-2}$ can be detected at $z > 6$. On the other hand, high-redshift AGN detections have been investigated by other theoretical models as well. At $z > 6$, to the flux limit of 3×10^{-17} erg cm $^{-2}$ s $^{-1}$ in the 0.2–2 keV band, optimistic detection of 500–600 AGNs per deg 2 and pessimistic detection of ~ 16 AGNs per deg 2 were predicted by Rhook & Haehnelt (2008) and Marulli et al. (2008), respectively. Although Marulli et al. (2008) successfully predicted the general BH mass function, they underestimated the number density of high- z bright AGNs when they used a constant Eddington accretion. While Rhook & Haehnelt (2008) extrapolated their merger-driven accretion model to high redshift for BH growth scenarios, and the predicted AGN numbers were sensitive on the early BH growth history. In our model, the BH accretion is adjusted by the BH mass. The value predicted in our model is two times larger than the value of Marulli et al. (2008), but 16–20 times smaller than the value of Rhook & Haehnelt (2008). All of these high-redshift predictions can be well verified by future observations.

4.6. Brief Illustration of Model Methodology

We use a simple analytical model to study the high-redshift AGN evolution in this paper. This model adopts some physical relations, such as $M_{\text{BH}} - \sigma$ and $\sigma - V_c$ relations, which are confirmed by observations and simulations. Because this is a phenomenological model, as discussed in previous subsections, some important physical properties related to the high-redshift AGN evolution, such as star formation, AGN/SN feedback, and BH accretion/merger, are not incorporated. However, semi-analytical models and hydro-dynamical simulations can self-consistently describe star formation, BH accretion, radiative cooling, and SN/AGN feedback processes under the framework of co-evolution between central BHs and their host galaxies.

In order to obtain enough spacial and mass resolutions of N-body simulations, especially for studying high redshift ($z > 7$) AGN evolutions, huge simulation box sizes and a large number of simulation particles inside each box are required. Hydro-dynamical simulations are also limited by the calculation grids in their computational domain. In the case of semi-analytical models, it usually takes heavy computational time to decide parameters for obtaining reasonable results. However, the calculations in our model have no limits on the box sizes, number of input particles, grids of the computational domain, and input parameters. This kind of phenomenological model can be applied as a preliminary test for semi-analytical models to comprehensively study the high-redshift AGN evolution. Furthermore, some interesting issues revealed in our model for the high-redshift AGN LFs, such as

the AGN flicker accretion and the AGN short lifetime, can be also noted and examined in purpose by semi-analytical models.

5. Conclusions

To investigate the evolution of AGNs at high redshift, we build a simple model to study high-redshift AGN LFs and AGN number counts. We have determined the following conclusions:

1. With a moderate sub-Eddington ratio and an AGN lifetime of about 10^7 - 10^8 years, optical and X-ray AGN LFs at high redshifts are produced. At $z \sim 4$, we do not obtain any flattening feature at the faint end of the optical AGN LF, consistent with observational results.
2. The optical AGN LF at $z = 6$ built by Willott et al. (2010a,b) and Kashikawa et al. (2014) can be reproduced with Eddington-limited accretion and an AGN lifetime of about 2×10^5 yrs. It seems possible that these AGNs at $z = 6$ are very young.
3. We calculate the X-ray AGN LFs at $2.0 < z < 5.0$ and the X-ray AGN number counts at $z > 3$ using the same parameters adopted for the calculation of the optical AGN LFs at $z \sim 4$. We estimate that, at $z > 6$, there are about 30 AGNs per deg^2 to the flux limit of $3 \times 10^{-17} \text{ erg cm}^{-2} \text{ s}^{-1}$ in the $0.5 - 2 \text{ keV}$ band.
4. High-redshift AGNs with central masses less than $10^8 M_\odot$ may dominate the cosmic reionization, though this domination is strongly dependent on the AGN LF, clumping factor, and escape fraction of ionizing photons.

Although our AGN LFs and AGN number counts at high redshifts have uncertainties that originate from the $M_{\text{BH}} - \sigma$ relation, Eddington ratio, AGN lifetime, and X-ray attenuation, they can be further constrained by optical and X-ray observations (Subaru/PFS, WFXT, eROSITA) in the future.

The observational data are kindly provided by J. Aird, A. Bongiorno, M. Brusa, F. Fontanot, E. Glikman, and L. Jiang. J. M. is grateful to X.-B. Wu, Y. Lu, W. Zuo, F. Fontanot, and Y. Ueda for their useful discussion. J.M. was encouraged by Shigehiro Nagataki for this work. J. M. is supported by the Hundred Talent Program of Chinese Academy of Sciences, the Major Project Program of Chinese Academy of Sciences (KJZD-EW-M06), and the Introducing Oversea Talent Plan of Yunnan Province. M. K. was supported by

Basic Science Research Program through the National Research Foundation (NRF) of Korea funded by the Ministry of Education, Science and Technology (2012-0001787).

A. Absorbed X-ray Spectral Templates

The observed AGN number counts in the X-ray band given by Brusa et al. (2009) and Civano et al. (2011) are related to the observed X-ray flux. Both the absorption N_{H} and the flux density of the X-ray spectrum in a given redshift should be determined to transform from intrinsic number counts to observed number counts.

In order to study the absorption feature of X-ray selected AGNs and obtain high-redshift AGN number counts in the X-ray band, we should investigate X-ray spectral templates at high redshifts. The model with command “*wabs * zwabs * pow*” can be used in XSPEC (version 12), as we assume that the spectrum can be fitted by an absorbed power-law. The Galactic absorption is taken as $N_{\text{H}} = 2.9 \times 10^{20} \text{ cm}^{-2}$ (Dickey & Lockman 1990). We assume a photon index $\Gamma = 2.0$ (Gilli et al. 2007) in the absorbed power-law spectrum. We show the X-ray spectra at redshifts 3, 4, 5, and 6 in Figure 12. Meanwhile, the spectra with the intrinsic absorption values of $N_{\text{H}} = 2.5 \times 10^{20}$, 5.0×10^{21} , 5.0×10^{22} , 5.0×10^{23} , and $2.5 \times 10^{24} \text{ cm}^{-2}$ are also given.

The normalized fluxes in the 0.5 – 2 keV band with a certain N_{H} can be obtained from the above spectral fitting. Using these spectral results, we quantitatively calculate the absorbed X-ray fluxes at high redshifts. Finally, as described in Section 2.2.2, the observed AGN number counts in the X-ray band can be derived.

B. BH–Halo Mass Relation and BH–Baryon Mass Relation

Although we focus on high-redshift AGN LFs and AGN number counts, we pay attention to the ratio of BH mass to dark matter halo mass and the ratio of BH mass to baryonic mass under the framework of joint evolution between AGNs and their host galaxies. We transfer dark matter halo mass to baryonic mass by a factor of 0.16. We show the plots of the BH–halo mass relation and the BH-baryon mass relation in Figures 13 and 14, respectively. In each Figure, the cases of redshift 4, 6, 8, and 9.5 are given. The different forms of the $M_{\text{BH}} - \sigma$ relation and the $M_{\text{BH}} - \sigma$ relation scatters are adopted in the calculations.

REFERENCES

- Aird, J., et al. 2010, MNRAS, 401, 2531
- Aird, J., et al. 2012, ApJ, 746, 90
- Aird, J., Coil, A. L., Georgakakis, A., Nandra, K., Baro, G., & Pérez-González, P. G. 2015, MNRAS, arXiv:1503.01120
- Antonucci, R. 2003, Annu. Rev. Astro. Astrophys., 31, 473
- Ballantyne, D. R., Everett, J. E., & Murray, N. 2006, ApJ, 639, 740
- Bajtlik, S., Duncan, R. C., & Ostriker, J. P. 1988, ApJ, 327, 570
- Batcheldor, D., et al. 2010, ApJ, 711, L108
- Barger, A. J., Cowie, L. L., Mushotzky, R. F., Yang, Y., Wang, W.-H., Steffen, A. T., & Capak, P. 2005, AJ, 129, 578
- Barton, E. J., Davé, R., Smith, J.-D. T., Papovich, C., Hernquist, L., & Springel, V. 2004, ApJ, 604, L1
- Begelman, M. C., & Nath, B. B. 2005, MNRAS, 361, 1387
- Bolton, J. S., Haehnelt, M. G., Warren, S. J., Hewett, P. C., Mortlock, D. J., Venemans, B. P., McMahon, R. G., & Simpson, C. 2011, MNRAS, 416, 70
- Bongiorno, A., et al. 2007, A&A, 472, 443
- Bournaud, F., Dekel, A., Teyssier, R., Cacciato, M., Daddi, E., Juneau, S., & Shankar, F. 2011, ApJ, 741, L33
- Bouwens, R. J., Illingworth, G. D., Blakeslee, J. P., & Franx, M. 2006, ApJ, 653, 53
- Bouwens, R. J., et al. 2011, Nature, 469, 504
- Bouwens, R. J., et al. 2015, arXiv:1503.08228
- Boyle, B. J., Shanks, T., Croom, S. M., Smith, R. J., Miller, L., Loaring, N. S., & Heymans, C., 2000, MNRAS, 317, 1014
- Brightman, M., Nandra, K., Salvato, M., Hsu, L.-T., Rangel, C. 2014, MNRAS, arXiv:1406.4502

- Brusa, M., et al. 2009, *ApJ*, 693, 8
- Brusa, M., et al. 2010, *ApJ*, 716, 348
- Bunker, A. J., et al. 2010, *MNRAS*, 409, 855
- Chou, R. C. Y., Bridge, C. R., & Abraham, R. G. 2011, *MNRAS*, 141, 87
- Choudhury, T. R., & Ferrara, A. 2005, *MNRAS*, 361, 577
- Ciotti, L. & Ostriker, J. P. 1997, *ApJ*, 487, L105
- Ciotti, L., Ostriker, J. P., & Proga, D. 2009, *ApJ*, 699, 89
- Civano, F., et al. 2011, *ApJ*, arXiv: 1103.2570
- Comastri, A., et al. 2010a, *A&A*, 526, L9
- Comastri, A., Ranalli, P., Gilli, R., Vignali, C., Brusa, M., & Civano, F. 2010, *Memorie della Società Astronomica Italiana* 2010, arXiv: 1011.1075
- Cowie, L. L., Songaila, A., Hu, E. M., Cohen, J. G. 1996, *AJ*, 112, 839
- Cowie, L. L., Barger, A. J., Bautz, M. W., Brandt, W. N., & Garmire, G. P. 2003, *ApJ*, 584, L57
- Cowie, L. L., Barger, A. J., & Hasinger, G. 2012, *ApJ*, 748, 50
- Cristiani, S., & Vio, R. 1990, *A&A*, 227, 385
- Cristiani, S., et al. 2004, *ApJ*, 600, L119
- Croom, S. M., Smith, R. J., Boyle, B. J., Shanks, T., Miller, L., Outtram, P. J., & Loaring, N. S. 2004, *MNRAS*, 349, 417
- Croom, S. M., et al. 2009, *MNRAS*, 399, 1755
- Croton, D. J., et al. 2006, *MNRAS*, 365, 11
- Croton, D. J. 2006, *MNRAS*, 394, 1109
- Davies, R. I., Mller Snchez, F., Genzel, R., Tacconi, L. J., Hicks, E. K. S., Friedrich, S., & Sternberg, A. 2007, *ApJ*, 671, 1388
- Decarli, R., Falomo, R., Treves, A., Labita, M., Kotilainen, J. K., & Scarpa, R. 2010, *MNRAS*, 402, 2453

- Dickey, J. M., & Lockman, F. J. ARA&A, 1990, 28, 215
- Dijkstra, M., Wyithe, J. S. B., & Haiman, Z. 2007, MNRAS, 379, 253
- Dudik, R. P., Satyapal, S., Gliozzi, M., & Sambruna, R. M. 2005, ApJ, 620, 113
- Ebrero, J., et al. 2009, A&A, 493, 55
- Elvis, M., et. al. 1994, ApJS, 95, 1
- Enoki, M., Ishiyama, T., Kobayashi, M. A. R., & Nagashima, M. 2014, ApJ, 794, 69
- Fabian, A. C. 1999, MNRAS, 308, L39
- Fabian, A. C., Vasudevan, R. V., Mushotzky, R. F., Winter, L. M., & Reynolds, C. S. 2009, MNRAS, 394, L89
- Fan, X., et al. 2001, AJ, 121, 54
- Fan, X., et al. 2002, AJ, 123, 124
- Fan, X., et al. 2006a, AJ, 132, 117
- Fan, X., Carilli, C. L., & Keating, B. 2006b, ARA&A, 44, 415
- Fanidakis, N., et al. 2010, MNRAS, 410, 53
- Fanidakis, N., et al. 2012, MNRAS, 419, 2797
- Ferrarese, L., & Merritt, D. 2000, ApJ, 539, L9
- Ferrarese, L. 2002, ApJ, 578, 90
- Fiore, F., et al. 2008, ApJ, 672, 94
- Fiore, F., et al. 2009, ApJ, 693, 447
- Fiore, F. 2010, Multiwavelength Approach and Future Perspectives, in the conference: "X-Ray Astronomy 2009 Present status, multi-wavelength approach and future perspectives", Bologna, arXiv: 1002.3538
- Fiore, F., et al. 2012, A&A, 537, A16
- Fontanot, F., Monaco, P., Cristiani, S., & Tuzzi, P. 2006, MNRAS, 373, 1173

- Fontanot, F., Cristiani, S., Monaco, P., Nonino, M., Vanzella, E., Brandt, W. N., Grazian, A., & Mao, J. 2007, *A&A*, 461, 39
- Gabor, J. M., & Bournaud, F., 2013, *MNRAS*, 434, 606
- Gebhardt, K., et al. 2000, *AJ*, 119, 1157
- Giallongo, E., et al. 2015, *A&A*, 578, A83
- Gilli, R., Risaliti, G., Severgnini, P., Maiolino, R., Marconi, A., & Salvati, M. 2001, *ASPC*, 234, 459
- Gilli, R., Comastri, A., & Hasinger, G. 2007, *A&A*, 463, 79
- Gilli, R., et al. 2011, *Memorie della Società Astronomica Italiana*, 17, 85
- Gilli, R., et al. 2011, *ApJ*, 730, L28
- Glikman, E., Bogosavljević, M., Stern, D., Dey, A., Jannuzi, B. T., & Mahabal, A. 2010, *ApJ*, 710, 1498
- Glikman, E., Djorgovski, S. G., Stern, D., Dey, A., Jannuzi, B. T., & Lee, K.-S. 2011, *ApJ*, 728, L26
- Granato, G. L., De Zotti, G., Silva, L., Bressan, A., & Danese, L., 2004, *ApJ*, 600, 580
- Greene, J. E., & Ho, L. C. 2007, *ApJ*, 670, 92
- Grupe, D., & Mathur, S. 2004, *ApJ*, 606, L41
- Gültekin, K., et al. 2009, *ApJ*, 698, 198
- Gunn, J. E., & Peterson, B. A. 1965, *ApJ*, 142, 1633
- Haehnelt, M. G., & Rees, M. J. 1993, *MNRAS*, 263, 168
- Haehnelt, M. G., Natarajan, P., & Rees, M. J. 1998, *MNRAS*, 300, 817
- Haiman, Z., & Loeb, A., 1998, *ApJ*, 503, 505
- Haiman, Z., & Hui, L., 2001, *ApJ*, 547, 27
- Haiman, Z., & Cen, R., 2002, *ApJ*, 578, 702
- Hao, J.-M., Yuan, Y.-F., & Wang, L. 2015, *MNRAS*, 451, 1875

- Haring, N., & Rix, H.-W. 2004, *ApJ*, 604, 89
- Hasinger, G., Miyaji, T., & Schmidt, M. 2005, *A&A*, 441, 417
- Hasinger, G. 2008, *A&A*, 490, 905
- Heckman, T. M., Kauffmann, G., Brinchmann, J., Charlot, S., Tremonti, C., White, S. D. M. 2004, *ApJ*, 613, 109
- Hickox, R. C., Mullaney, J. R., Alexander, D. M., Chen, C.-T. J., Civano, F. M., Goulding, A. D., & Hainline, K. N. 2014, *ApJ*, 782, 9
- Hicks, E. K. S., Davies, R. I., Malkan, M. A., Genzel, R., Tacconi, L. J., Müller Sánchez, F., & Sternberg, A. 2009, *ApJ*, 696, 448
- Hiroi, K., Ueda, Y., Akiyama, M., Watson, M. G. 2012, *ApJ*, 758, 49
- Hirschmann, M., Somerville, R. S., Naab, T., & Burkert, A. 2012, *MNRAS*, 426, 237
- Hirschmann, M., Dolag, K., Saro, A., Bachmann, L., Borgani, S. & Burkert, A. 2014, *MNRAS*, 442, 2304
- Hopkins, P. F., Hernquist, L., Cox, T. J., Di Matteo, T., Robertson, B., & Springel, V. 2005, *ApJ*, 632, 81
- Hopkins, P. F., Richards, G. T., & Hernquist, L. 2007, *ApJ*, 654, 731
- Hopkins, P. F., & Hernquist, L. 2009, *ApJ*, 698, 1550
- Hopkins, P. F., Hickox, R., Quataert, E., & Hernquist, L. 2009, *MNRAS*, 398, 333
- Hopkins, P. F., Hayward, C. C., Narayanan, D., & Hernquist, L. 2011, arXiv: 1108.3086
- Iliev, I. T., Mellema, G., Pen, U.-L., Merz, H., Shapiro, P. R., & Alvarez, M. A. 2006, *MNRAS*, 369, 1625
- Ikeda, H. et al. 2011, *ApJ*, 728, L25
- Jiang, L., et al. 2009, *AJ*, 138, 305
- Jiang, L., et al. 2010, *Nature*, 464, 380
- Kashikawa, N., et al. 2014, *ApJ*, arXiv: 1410.7401
- Kauffmann, G., & Heckman, T. M. 2009, *MNRAS*, 397, 135

- Kaurov, A. A., & Gnedin, N. Y. 2014, *ApJ*, arXiv:1412.5607
- Kawakatu, N., Umemura, M., & Mori, M. 2002, *ApJ*, 583, 85
- King, A. 2003, *ApJ*, 596, L27
- King, A. 2005, *ApJ*, 635, L121
- King, A. 2010, *MNRAS*, 408, L95
- Kitayama, T., & Suto, Y. 1996, *MNRAS*, 280, 638
- Kollmeier, J. A., et al. 2006, *ApJ*, 648, 128
- Kormendy, J., & Bender, R. 2011, *Nature*, 469, 377
- Kulkarni, G., & Loeb, A. 2011, arXiv: 1107.0517
- Lamastra, A., Menci, N., Maiolino, R., Fiore, F., & Merloni, A. 2010, *MNRAS*, 405, 29
- Lawrence, A. 1991, *MNRAS*, 252, 586
- La Franca, F., et al. 2005, *ApJ*, 635, 864
- Lanzuisi, G., et al. 2014, *A&A*, arXiv: 1409.1867
- Lapi, A., Shankar, F., Mao, J., Granato, G. L., Silva, L., De Zotti, G., & Danese, L. 2006, *ApJ*, 650, 42
- Lapi, A., Raimundo, S., Aversa, R., Cai, Z.-Y., Negrello, M., Celotti, A., De Zotti, G., & Danese, L. 2014, *ApJ*, 782, 69
- Lemaux, B. C., et al. 2014, *A&A*, arXiv: 1311.5228
- Loeb, A., & Peebles, P. J. E. 2003, *ApJ*, 589, 29
- Lu, Y., & Yu, Q. 2011, *ApJ*, 736, 49
- Madau, P., Haardt, F., & Rees, M. J. 1999, *ApJ*, 514, 648
- Magorrian, J., et al. 1998, *AJ*, 115, 2285
- Mahmood, A., Devriendt, J. E., & Silk, J. 2005, *MNRAS*, 359, 1363
- Maiolino, R., Schneider, R., Oliva, E., Bianchi, S., Ferrara, A., Mannucci, F., Pedani, M., & Roca Sogorb, M. 2004, *Nature*, 431, 533

- Mao, J., Lapi, A., Granato, G. L., de Zotti, G., & Danese, L. 2007, *ApJ*, 667, 655
- Marconi, A., & Hunt, L. K. 2003, *ApJ*, 589, L21
- Marconi, A., Risaliti, G., Gilli, R., Hunt, L. K., Maiolino, R., & Salvati, M. 2004 *MNRAS*, 351, 169
- Marulli, F., Bonoli, S., Branchini, E., Moscardini, L., & Springel, V. 2008, *MNRAS*, 385, 1846
- Masters, D., et al. 2012, *ApJ*, 755, 169
- Martini, P., & Weinberg, D. H. 2001, *ApJ*, 547, 12
- Matt, G. 2002, *ASP Conf. Ser.*, 258, 3
- Mayo, J. H., Lawrence, A. 2013, *MNRAS*, 434, 1593
- McGreer, I. D., et al. 2013, *ApJ*, 768, 105
- McLure, R. J., Jarvis, M. J., Targett, T. A., Dunlop, J. S., & Best, P. N. 2006, *MNRAS*, 368, 1395
- Meiksin, A. 2005, *MNRAS*, 356, 596
- Menci, N., Fiore, F., Puccetti, S., & Cavaliere, A. 2008, *ApJ*, 686, 219
- Miyaji, T., Hasinger, G., & Schmidt, M. 2000, *A&A*, 353, 25
- Miyaji, T., Hasinger, G., & Schmidt, M. 2001, *A&A*, 369, 49
- Miyaji, T., et al. 2015, *ApJ*, arXiv:1503.00056
- Narayan, R., & Yi, I. 1995, *ApJ*, 428, L13
- Nayakshin, S., Wilkinson, M. I., & King, A. 2009, *MNRAS*, 398, L54
- Navarro, J. F., Frenk, C. S., & White, S. D. M. 1997, *ApJ*, 490, 493
- Nelson, C. H., Green, R. F., Bower, G., Gebhardt, K., & Weistrop, D. 2004, *ApJ*, 615, 652
- Novak, G. S., Ostriker, J. P., & Ciotti, L., *ApJ*, 737, 26
- Press, W. H., & Schechter, P. L. 1974, *ApJ*, 181, 425
- Reed, S. L., et al. 2015, arXiv:1504.03264

- Rhook, K. J., & Haehnelt, M. G. 2008, MNRAS, 389, 270
- Richstone, D., et al. 1998, Nature, 395, 14
- Risaliti, G., Maiolino, R., & Salvati, M. 1999, ApJ, 522, 157
- Robertson, B., Hernquist, L., Cox, T. J., Di Matteo, T., Hopkins, P. P., Martini, P., & Springel, V. 2006, ApJ, 641, 90
- Robertson, B. E., Ellis, R. S., Dunlop, J. S., McLure, R. J., & Stark, D. P. 2010, Nature, 468, 55
- Rosati, P., et al. 2010, Memorie della Società Astronomica Italiana 2010, arXiv: 1010.6252
- Salpeter, E. E. 1964, ApJ, 140, 796
- Salvaterra, R., Ferrara, A., & Dayal, P. 2011, MNRAS, 414, 847
- Sasaki, S. 1994, PASJ, 46, 427
- Schawinski, K., Koss, M., Berney, S., & Sartori, L. F. 2015, MNRAS, 451, 2517
- Schulze, A. & Wisotzki, L. 2014, MNRAS, 438, 3422
- Shakura, N. I., & Sunyaev, R. A. 1973, A&A, 24, 337
- Shankar, F., & Mathar, S. 2007, ApJ, 660, 1051
- Shankar, F., Bernardi, M., & Haiman, Z. 2009a, ApJ, 694, 867
- Shankar, F., Weinberg, D. H., & Miralda-Escudé, J. 2009b, ApJ, 690, 20
- Shankar, F., Croce, M., Miralda-Escudé, J., Fosalba, P. & Weinberg, D. H. 2010, ApJ, 718, 231
- Shankar, F., Weinberg, D. H., Miralda-Escudé, J. 2013, MNRAS, 428, 421
- Shapiro, P. R., & Giroux, M. L. 1987, ApJ, 321, L107
- Shen, Y. 2009, ApJ, 704, 89
- Sheth, R. K., & Tormen, G. 1999, MNRAS, 308, 119
- Sheth, R. K., & Tormen, G. 2002, MNRAS, 329, 61
- Shemmer, O., Brandt, W. N., Netzer, H., Maiolino, R., & Kaspi, S. 2006, ApJ, 646, L29

- Shi, Y., et al. 2006, ApJ, 653, 127
- Shields, G. A., Gebhardt, K., Salviander, S., Wills, B. J., Xie, B., Brotherton, M. S., Yuan, J., & Dietrich, M. 2003, ApJ, 583, 124
- Shields, G. A., Menezes, K. L., Massart, C. A., & Vanden Bout, P. 2006, ApJ, 641,683
- Silk, J., & Rees, M. J. 1998, A&A, 331, L1
- Small, T. A., & Blandford, R. D. 1992, MNRAS, 259, 725
- Somerville, R. S. 2009, MNRAS, 399, 1988
- Spergel, D. N., et al. 2006, ApJS, 170, 277
- Springel, V., et al. 2005, Nature, 435, 629
- Steidel, C. C., Adelberger, K. L., Shapley, A. E., Dickinson, M., Pettini, M., Giavalisco, M. 2003, ApJ, 592, 728
- Tanaka, T., Perna, R., & Haiman, Z. 2012, MNRAS, 425, 2974
- Tozzi, P., et al. 2006, A&A, 451, 457
- Treister, E., Schawinski, K., Volonteri, M., Natarajan, P., & Gawiser, E. 2011, Nature, 474, 356
- Tremaine, S., et al. 2002, ApJ, 574, 740
- Ueda, Y., Akiyama, M., Ohta, K., & Miyaji, T. 2003, ApJ, 598, 886
- Ueda, Y., Akiyama, M., Hashinger, G., Miyaji, T., Watson, M. 2014, ApJ, 786, 104
- Valiante, R., Schneider, R., Bianchi, S., & Andersen, A. C. 2009, MNRAS, 397, 166
- Valiante, R., Schneider, R., Salvadori, S., & Bianchi, S. 2011, MNRAS, 416, 1916
- van Dokkum, P. G., et al. 2005, AJ, 130, 2647
- Venemans, B. P., et al. 2015, ApJ, 801, L11
- Volonteri, M., & Gnedin, N. Y. 2009a, ApJ, 703, 2113
- Volonteri, M., & Natarajan, P. 2009b, MNRAS, 400, 1911
- Volonteri, M., Natarajan, P., & Gültekin, K. 2011, ApJ, 737, 50

- Wada, K., Papadopoulos, P. P., & Spaans, M. 2009, *ApJ*, 702, 63
- Willott, C. J., et al. 2010a, *AJ*, 140, 546
- Willott, C. J., et al. 2010b, *AJ*, 139, 906
- Willott, C. J. 2011, *ApJ*, 742, L8
- Woo, J.-H., et al. 2010, *ApJ*, 716, 269
- Wu, X.-B. 2007, *ApJ*, 657, 177
- Wu, X.-B., et al. 2015, *Nature*, 518, 512
- Wyithe, J. S. B, & Loeb, A. 2002, *ApJ*, 581, 886
- Wyithe, J. S. B, & Loeb, A. 2003, *ApJ*, 595, 614
- Yenko, B., Barger, A. J., Trouille, L., & Winter, L. M. 2009, *ApJ*, 698, 380

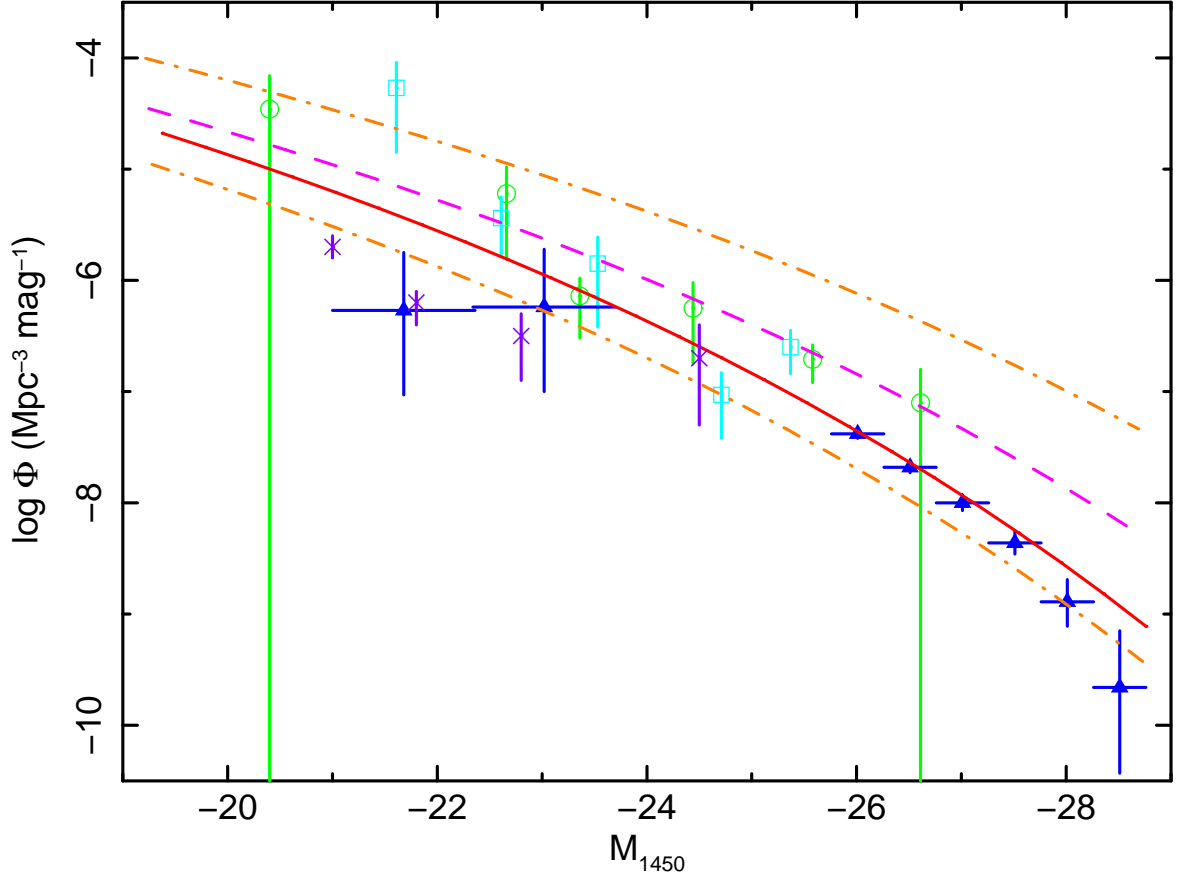


Fig. 1.— Optical AGN LFs at $z = 4$. Data points with error bars are collected from Fontanot et al. (2007) (solid triangles), Masters et al. (2012) (solid cross), and Glikman et al. (2010) (photometric-redshift selection results denoted by empty circles and spectral-redshift identification results denoted by empty squares). The solid line denotes our result, adopting the $M_{\text{BH}} - \sigma$ relation from numerical simulations given by Robertson et al. (2006). The dashed line denotes our result as well, adopting the observational $M_{\text{BH}} - \sigma$ relation given by Gültekin et al. (2009). Two dotted-dashed lines denote the lower and upper limits of our model results in the case where the intrinsic scatter of the observational $M_{\text{BH}} - \sigma$ relation given by Gültekin et al. (2009) is considered.

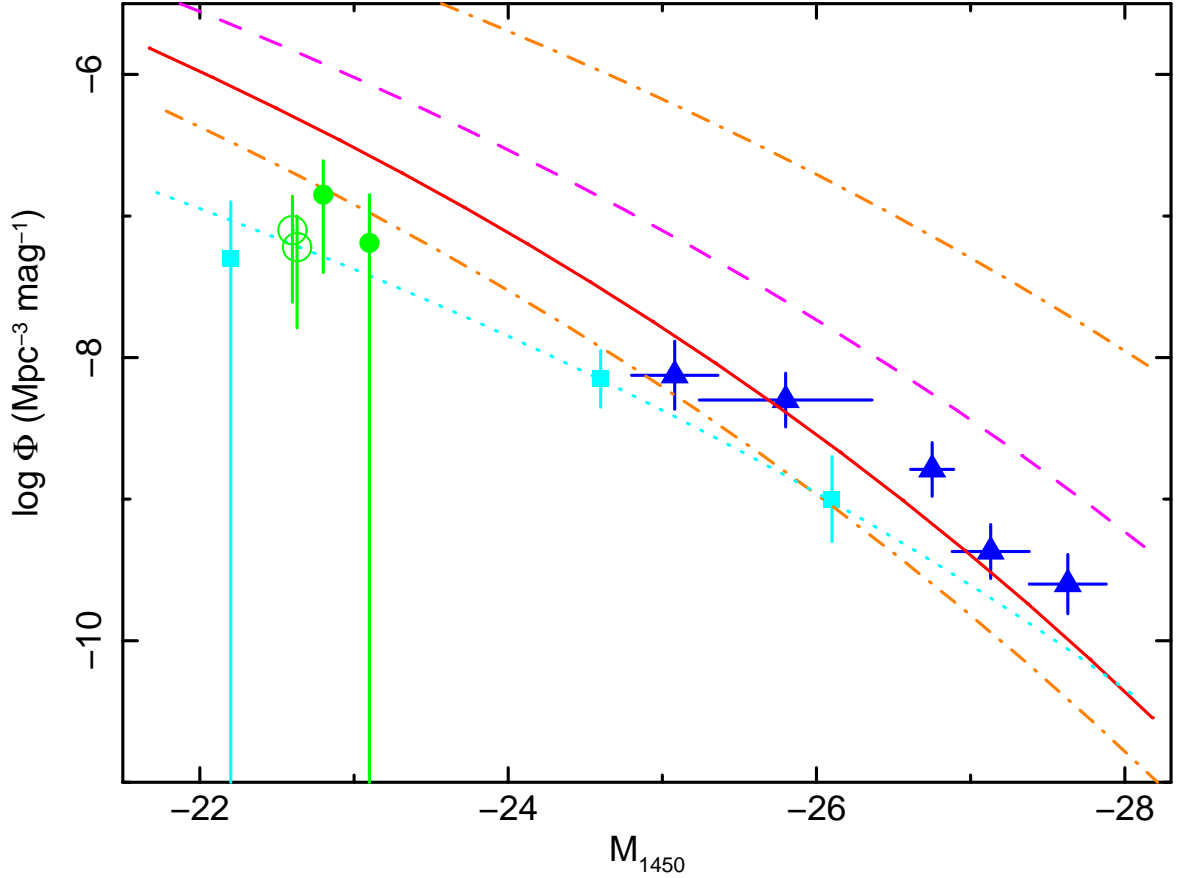


Fig. 2.— Optical AGN LFs at $z = 6$. Data points with error bars are collected from Jiang et al. (2009) (solid triangles), Willott et al. (2010b) (solid squares), and Kashikawa et al. (2014) (solid and empty circles). Those denotations of solid, dashed, and two dotted-dashed lines are the same as those in Figure 1. In particular, the dotted line indicates the result of the calculation with the Eddington ratio of $\lambda = 2.0(M_{\text{BH}}/2 \times 10^9 M_{\odot})^{0.5}$ and a very short AGN lifetime of 2×10^5 years. In this case, the $M_{\text{BH}} - \sigma$ relation given by Robertson et al. (2006) is adopted.

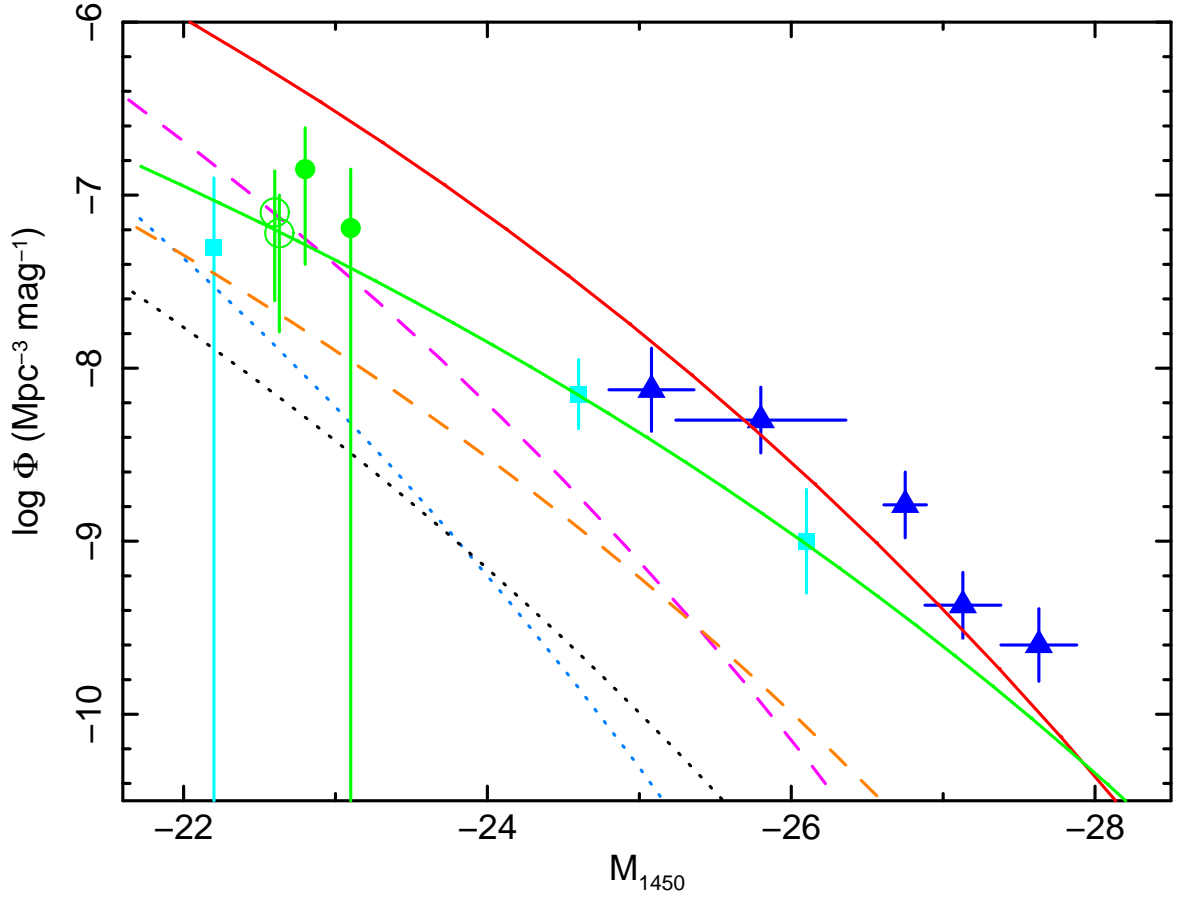


Fig. 3.— Optical AGN LFs at $z = 6$ (solid lines), $z = 8$ (dashed lines), and $z = 9.5$ (dotted lines), respectively. Red, pink, and blue lines indicate the results calculated from the sub-Eddington accretion of $\lambda = 0.25(M_{\text{BH}}/2 \times 10^9 M_{\odot})^{0.5}$ and the AGN lifetime of 2×10^7 years. Green, orange, and black lines indicate the results calculated from the Eddington accretion of $\lambda = 2.0(M_{\text{BH}}/2 \times 10^9 M_{\odot})^{0.5}$ and the AGN lifetime of 2×10^5 years. The $M_{\text{BH}} - \sigma$ relation from the numerical simulations given by Robertson et al. (2006) is used to reproduce all of these AGN LFs. Data points with error bars are the same as those in Figure 2.

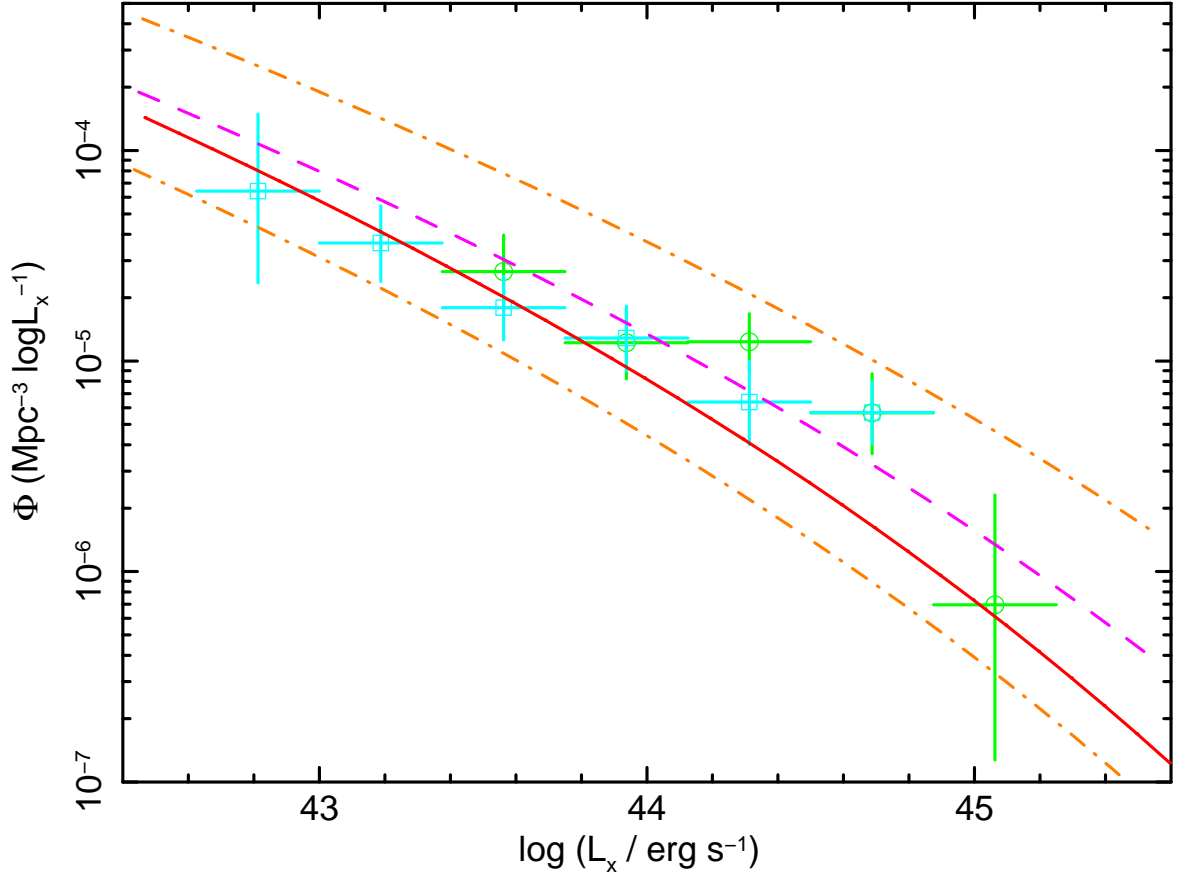


Fig. 4.— AGN LFs in the 2 – 10 keV band at $z = 2.25$. Data points with error bars are the observational results at $2.0 < z < 2.5$ given by Aird et al. (2010): open circles denote the AGN LF obtained with the X-ray selected sample while open squares denote the AGN LF obtained with the high-redshift color pre-selected sample. The solid line denotes our result, adopting the $M_{\text{BH}} - \sigma$ relation from the numerical simulations given by Robertson et al. (2006). The dashed line denotes our result as well, adopting the observational $M_{\text{BH}} - \sigma$ relation given by Gültekin et al. (2009). Two dotted-dashed lines denote the lower and upper limits of our results in the case that the intrinsic scatter of the observational $M_{\text{BH}} - \sigma$ relation given by Gültekin et al. (2009) is considered.

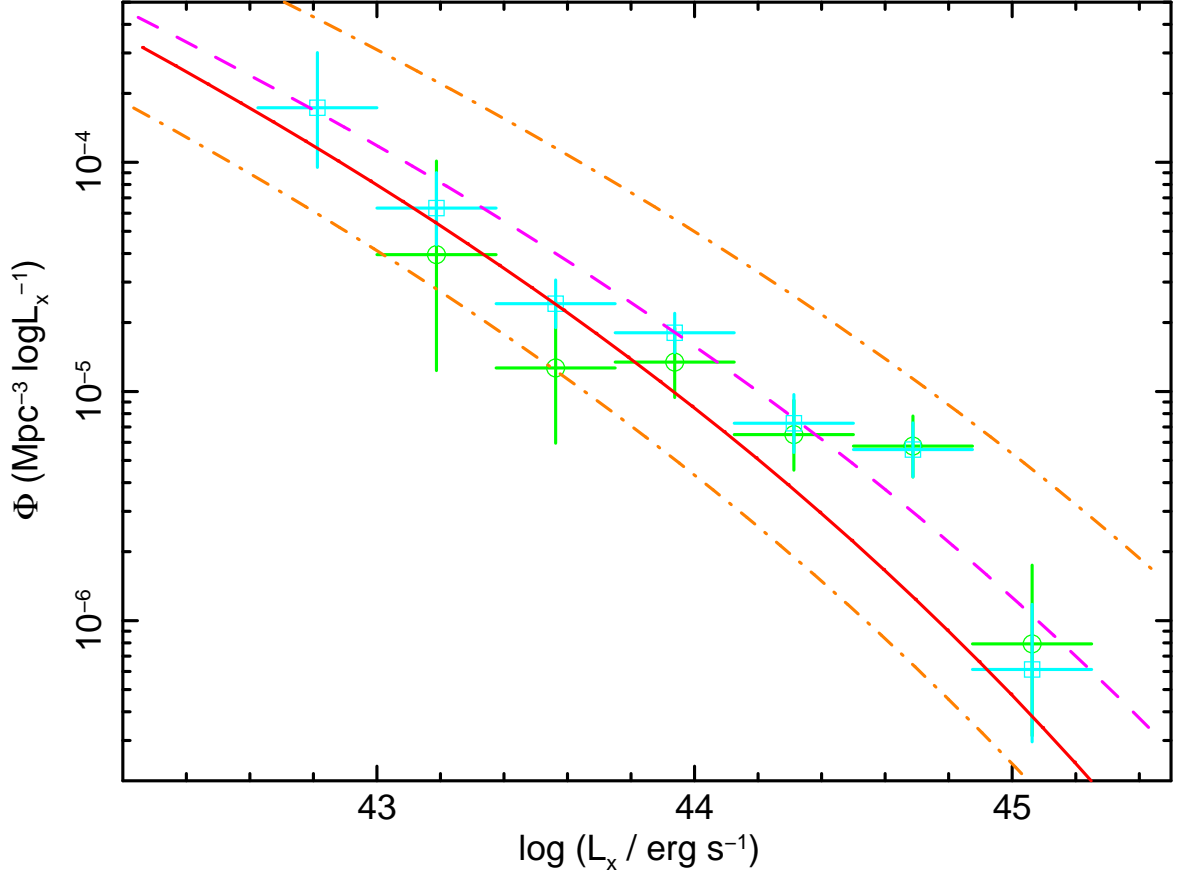


Fig. 5.— AGN LFs in the 2 – 10 keV band at $z = 3.0$. The data points with error bars are the observational results at $2.5 < z < 3.5$ given by Aird et al. (2010): the open circles denote the AGN LF obtained with the X-ray selected sample while the open squares denote the AGN LF obtained with the high-redshift color pre-selected sample. The denotations of solid, dashed, and two dot-dashed lines are the same as those in Figure 4.

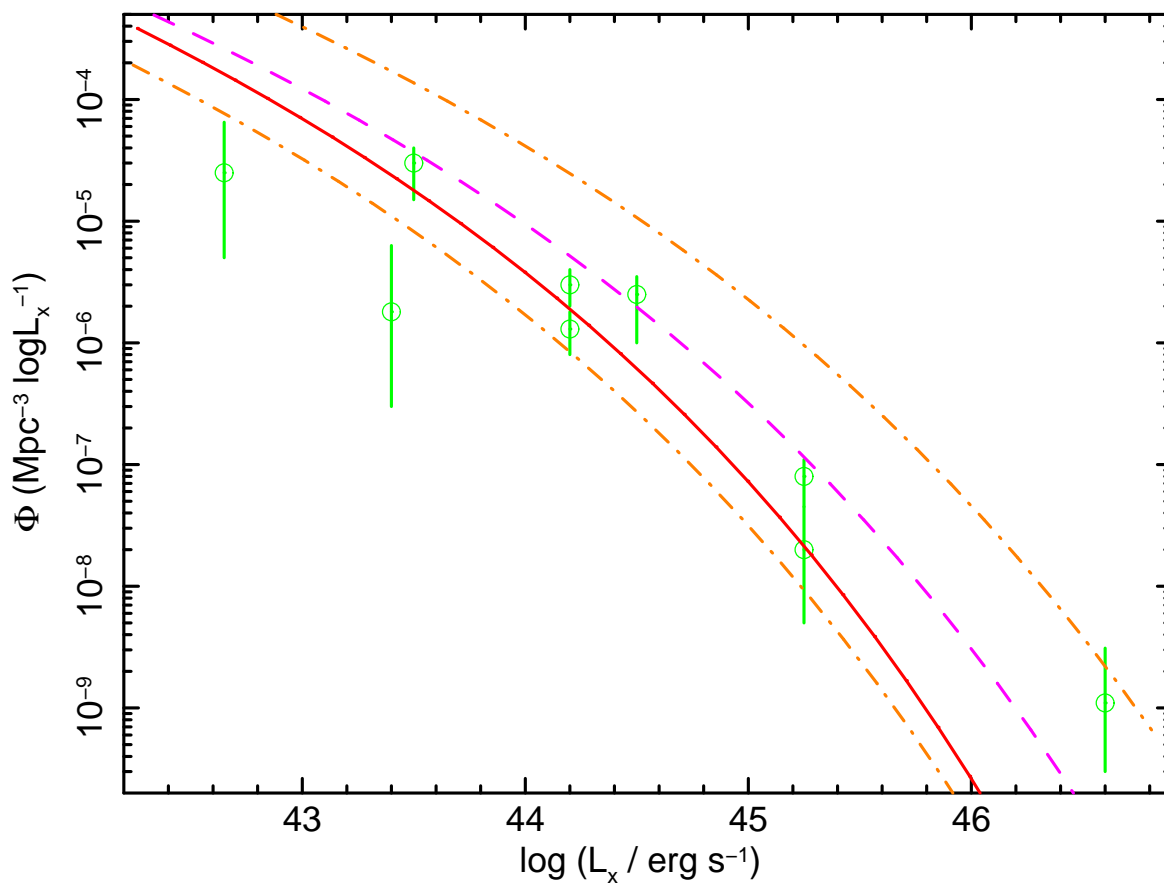


Fig. 6.— AGN LFs in the 2 – 10 keV band at $z = 4.5$. The data points with error bars are the observational results at $4.0 < z < 5.0$ given by Ueda et al. (2014). The denotations of solid, dashed, and two dotted-dashed lines are the same as those in Figure 4.

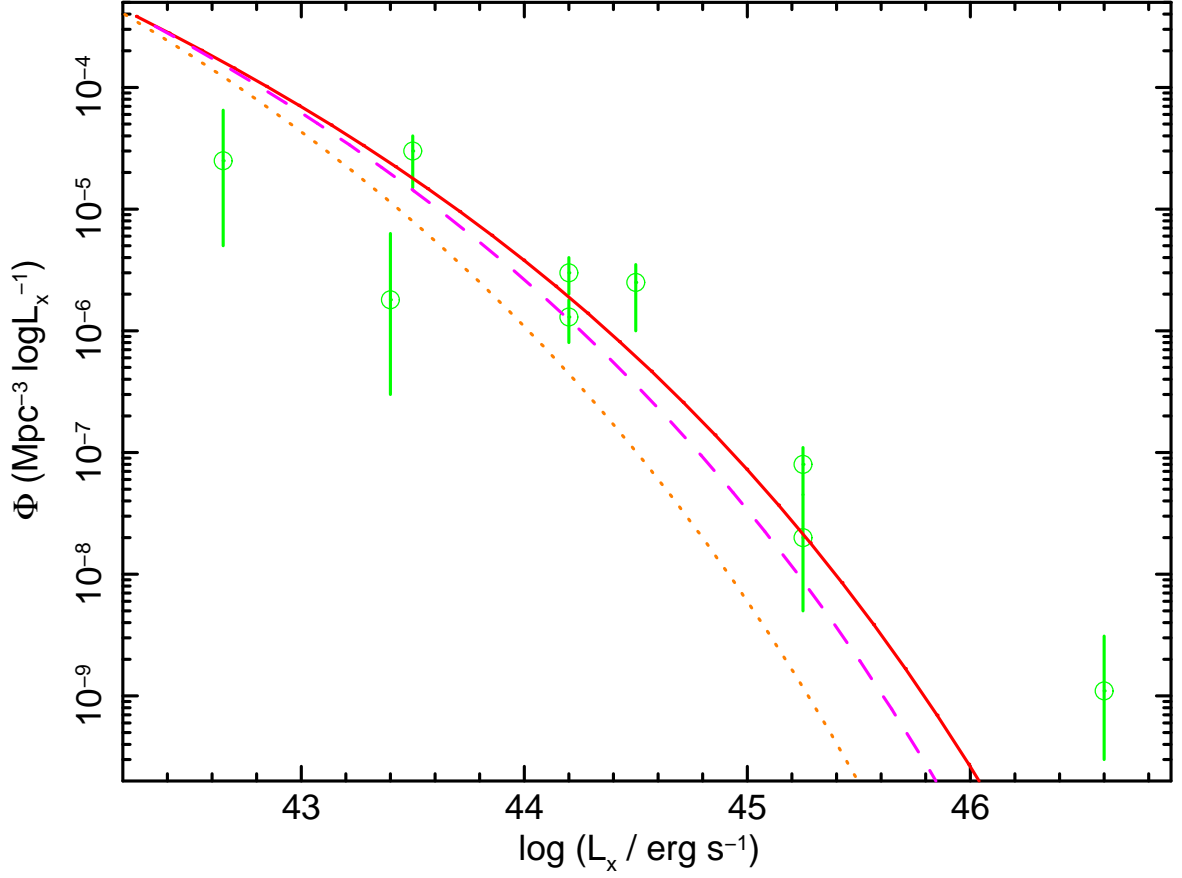


Fig. 7.— AGN LFs in the 2 – 10 keV band at $z = 4.5$ (solid line), $z = 5$ (dashed line), and $z = 6$ (dotted line), respectively. The $M_{\text{BH}} - \sigma$ relation given by Robertson et al. (2006) is considered to reproduce these AGN LFs. Data points with error bars are the observational AGN LFs given by Ueda et al. (2014) at $4.0 < z < 5.0$.

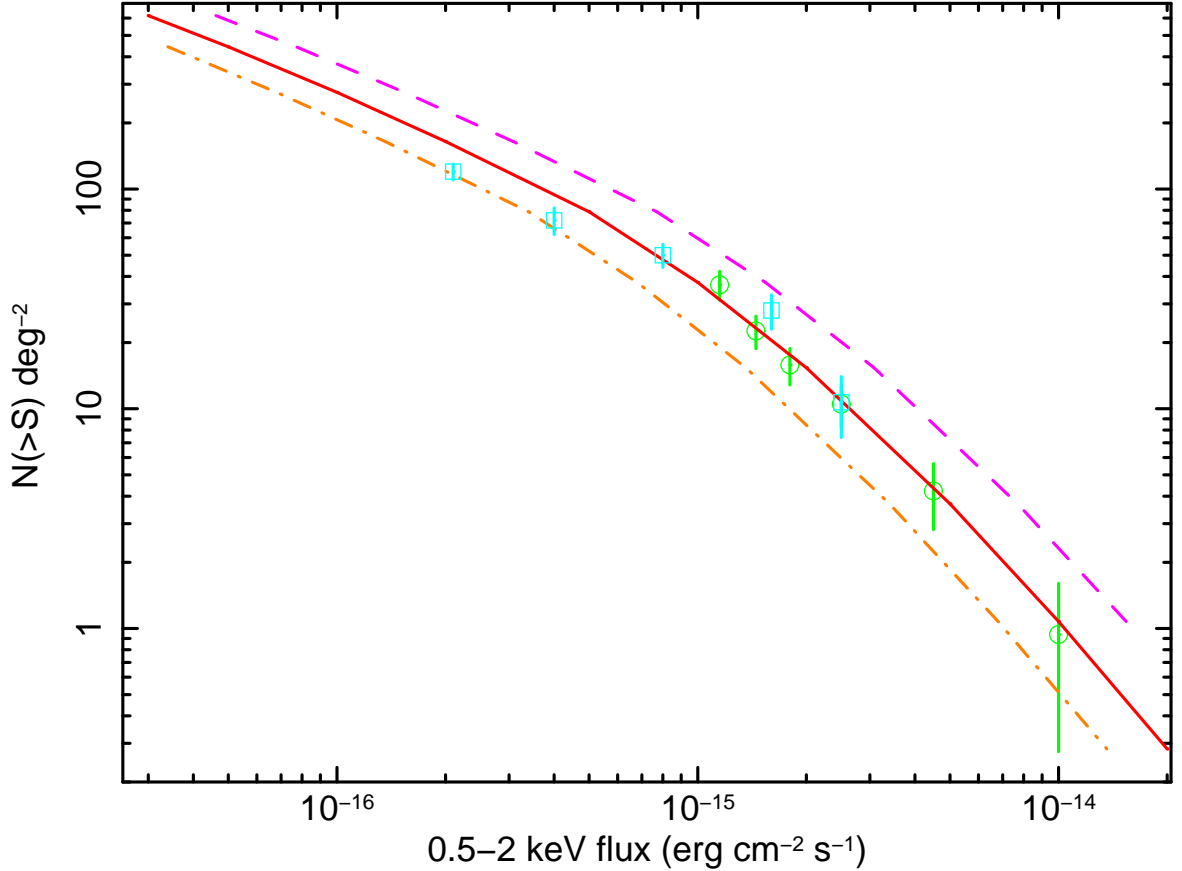


Fig. 8.— AGN number counts in the 0.5 – 2 keV band at $z > 3$. Data points with error bars denoted by circles and squares are those observational results from the XMM-COSMOS survey (Brusa et al. 2009) and the *Chandra*-COSMOS survey (Civano et al. 2011), respectively. Solid, dashed, and dotted-dashed lines denote our results with N_{H} values of $5.0 \times 10^{22} \text{ cm}^{-2}$, $1.0 \times 10^{22} \text{ cm}^{-2}$, and $1.0 \times 10^{23} \text{ cm}^{-2}$, respectively. The $M_{\text{BH}} - \sigma$ relation from the numerical simulations given by Robertson et al. (2006) is considered in our calculations.

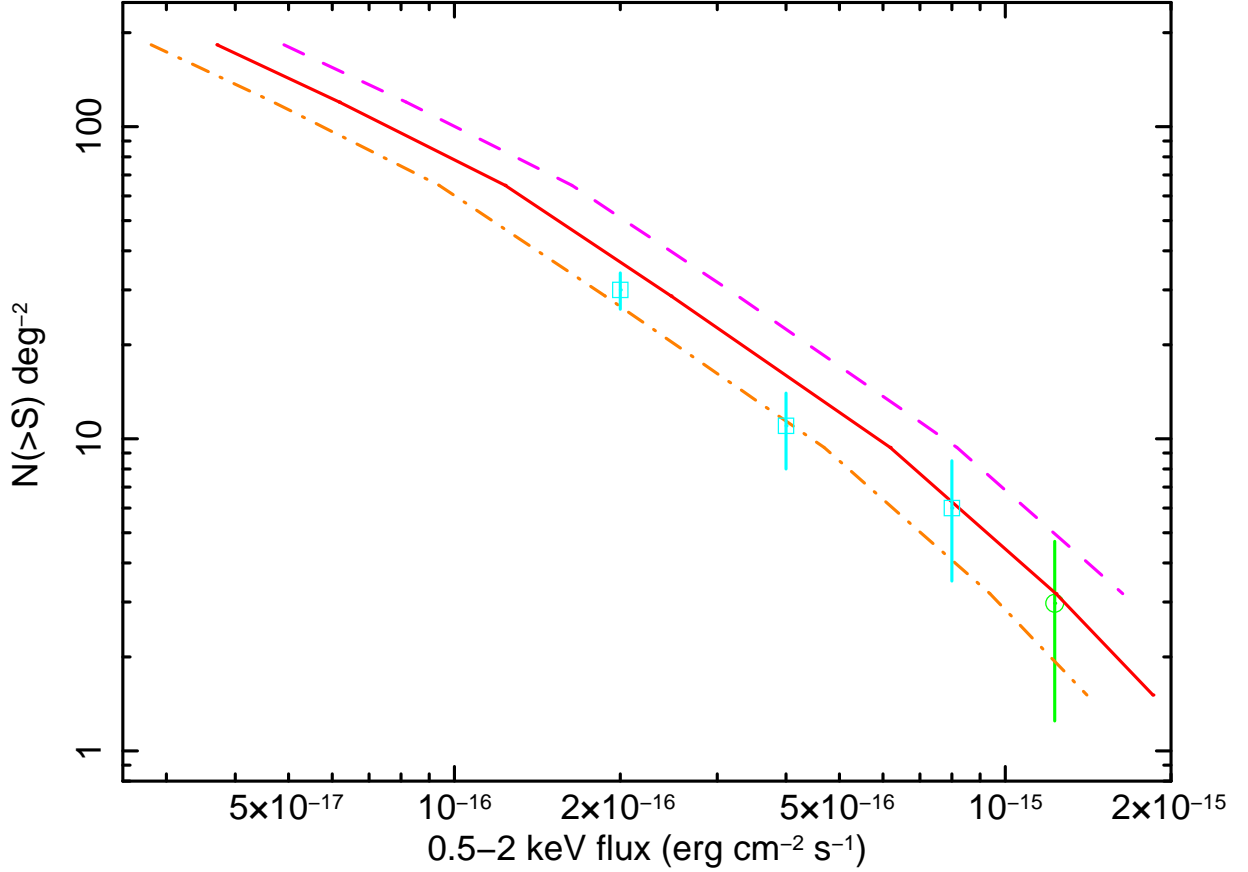


Fig. 9.— AGN number counts in the 0.5 – 2 keV band at $z > 4$. Data points with error bars denoted by circles and squares are the observational results from the XMM-COSMOS survey (Brusa et al. 2009) and the *Chandra*-COSMOS survey (Civano et al. 2011), respectively. The denotations of solid, dashed, and dot-dashed lines are the same as those in Figure 8. The $M_{\text{BH}} - \sigma$ relation from the numerical simulations given by Robertson et al. (2006) is considered in our calculations.

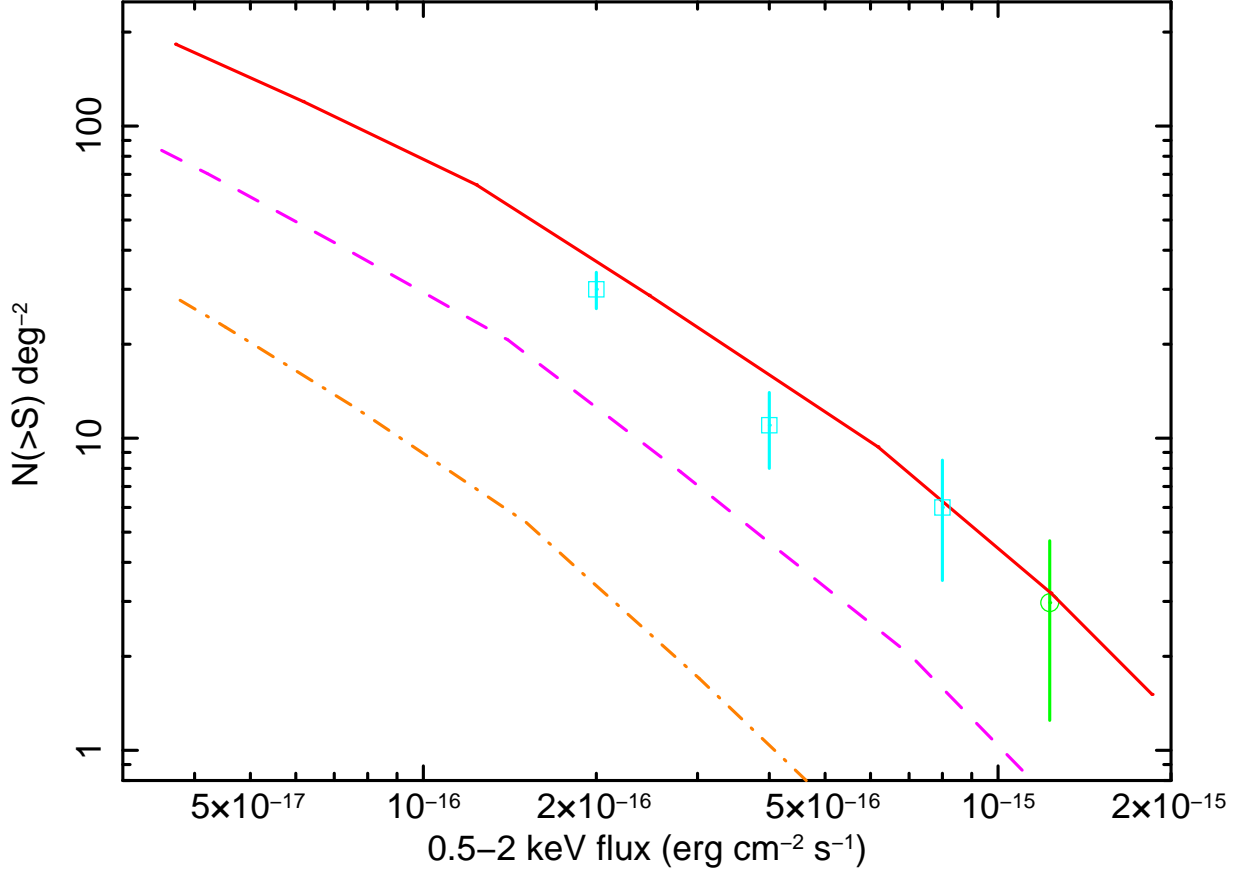


Fig. 10.— AGN number counts in the 0.5 – 2 keV band at $z > 4$ (solid line), $z > 5$ (dashed line), and $z > 6$ (dotted-dashed line), respectively. The theoretical $M_{\text{BH}} - \sigma$ relation given by Robertson et al. (2006) and the absorption of $N_{\text{H}} = 5.0 \times 10^{22} \text{ cm}^{-2}$ are considered. Data points with error bars denoted by circles and squares are the same as those in Figure 9.

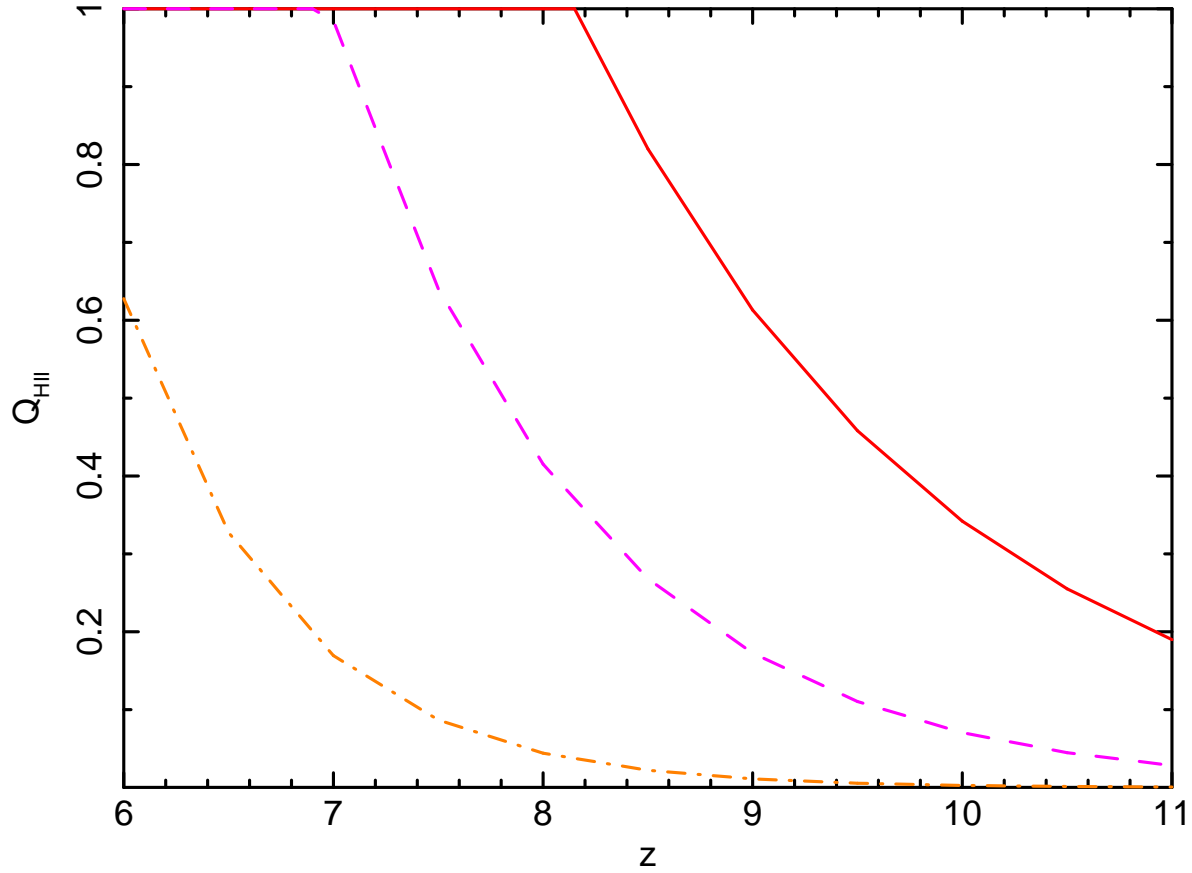


Fig. 11.— Evolution of filling factor Q_{HII} . Solid, dashed and dotted-dashed lines denote our results from the contributions of BHs with mass ranges of $10^6 - 10^7 M_{\odot}$, $10^7 - 10^8 M_{\odot}$, and $10^8 - 10^9 M_{\odot}$, respectively.

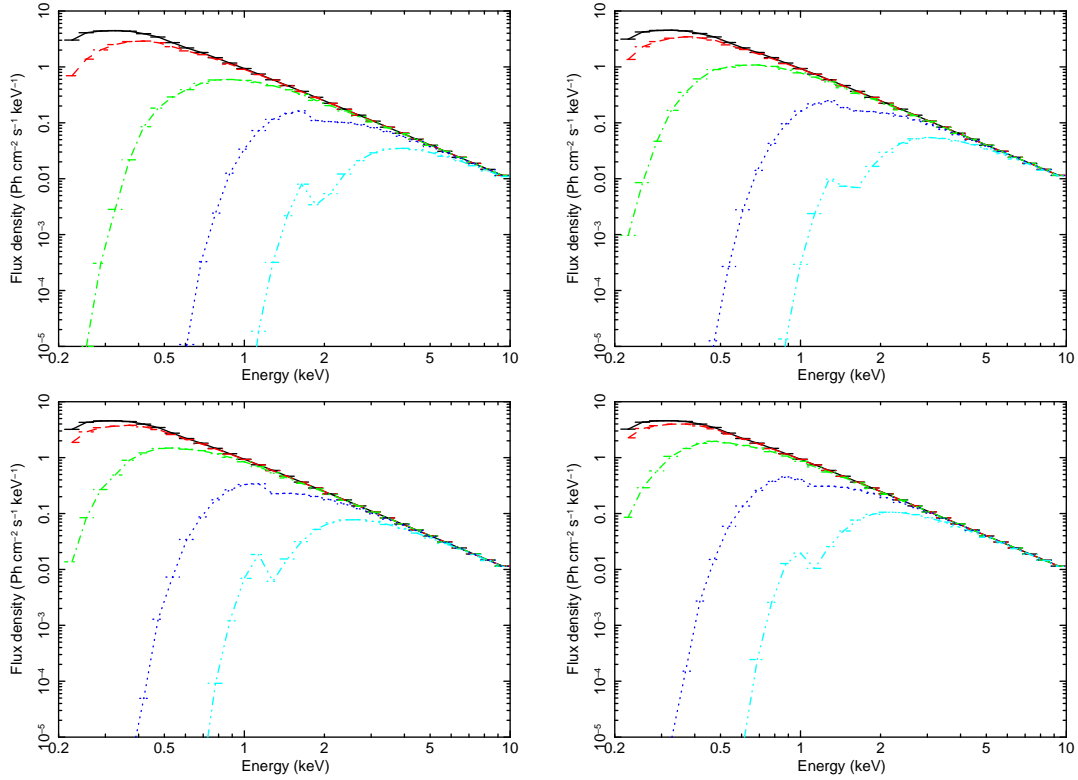


Fig. 12.— Absorbed spectral templates in the X-ray band. Several cases of different N_{H} values ($2.9 \times 10^{20} \text{ cm}^{-2}$, $5.0 \times 10^{21} \text{ cm}^{-2}$, $5.0 \times 10^{22} \text{ cm}^{-2}$, $5.0 \times 10^{23} \text{ cm}^{-2}$, and $2.5 \times 10^{24} \text{ cm}^{-2}$) are denoted by a solid line, dashed line, dotted-dashed line, dotted line, and dotted-dotted-dotted-dashed line, respectively. Top-left panel: spectra at $z = 3$; Top-right panel: spectra at $z = 4$; Bottom-left panel: spectra at $z = 5$; Bottom-right panel: spectra at $z = 6$.

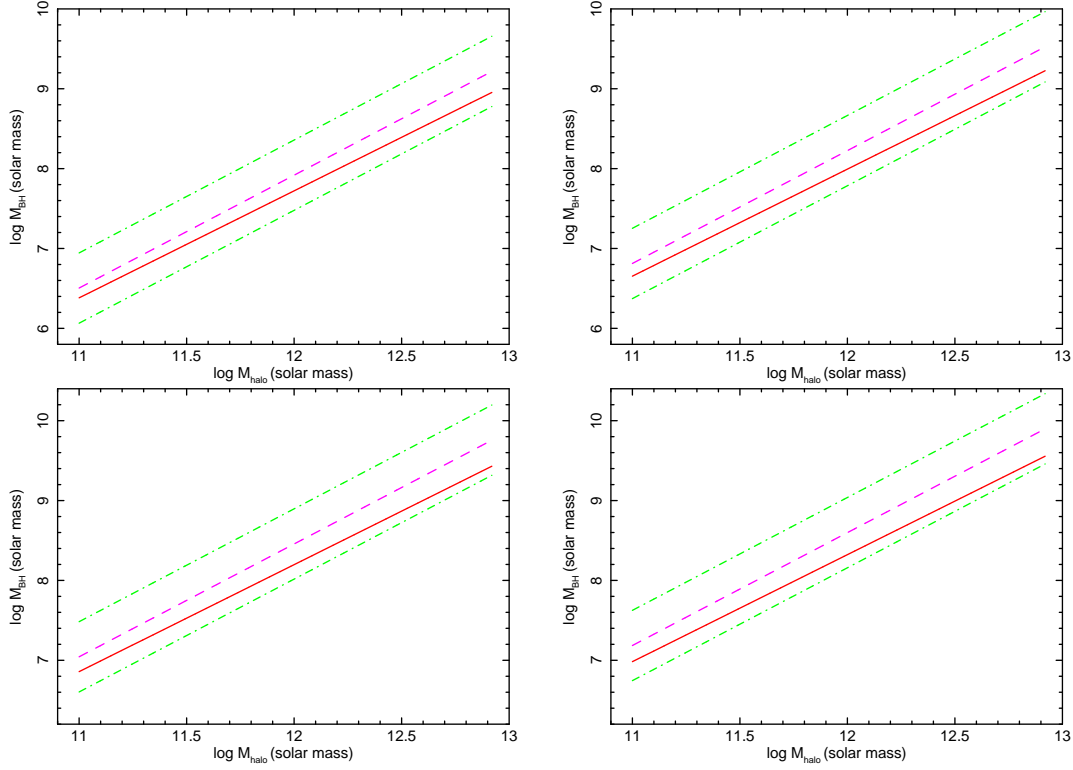


Fig. 13.— BH–Halo mass relation. The solid line denotes our result, adopting the $M_{\text{BH}} - \sigma$ relation from the numerical simulation given by Robertson et al. (2006). The dashed line denotes our result, adopting the observational $M_{\text{BH}} - \sigma$ relation given by Gültekin et al. (2009). The two dotted-dashed lines denote the lower and upper limits of our results in the case in which the intrinsic scatter of the observational $M_{\text{BH}} - \sigma$ relation given by Gültekin et al. (2009) is considered. top-left panel: relation at $z = 4$; top-right panel: relation at $z = 6$; bottom-left panel: relation at $z = 8$; bottom-right panel: relation at $z = 9.5$.

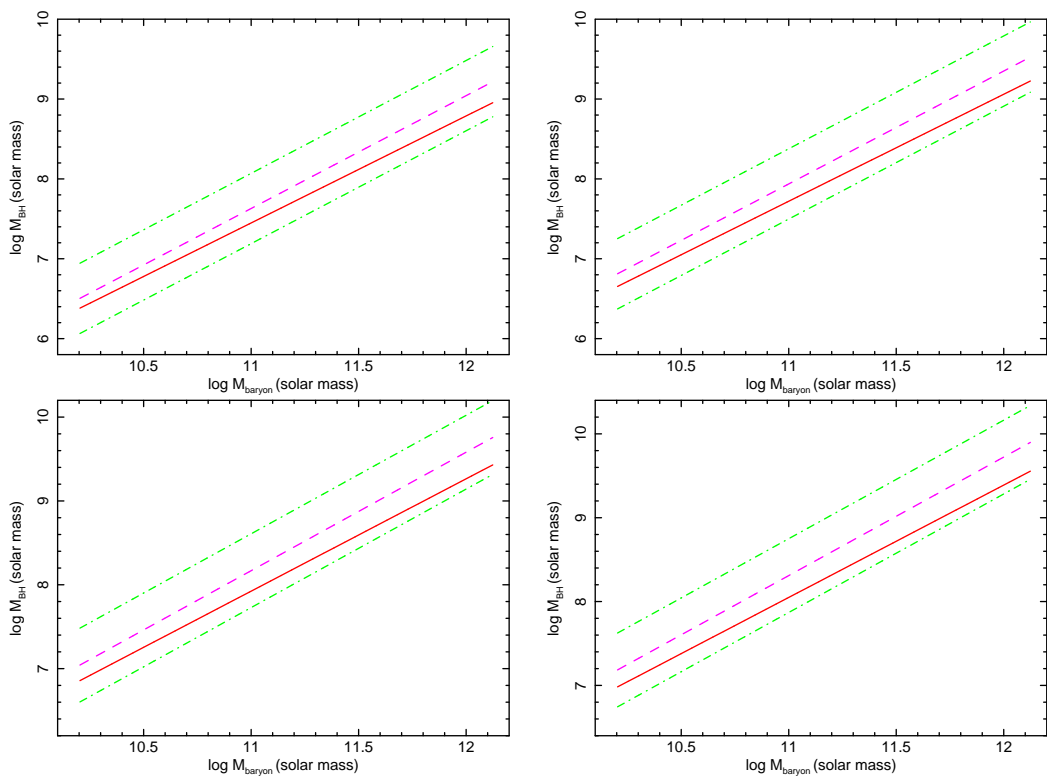


Fig. 14.— BH–baryon mass relation. The denotations of solid, dashed, and two dotted-dashed lines are the same as those in Figure 13. top-left panel: relation at $z = 4$; top-right panel: relation at $z = 6$; bottom-left panel: relation at $z = 8$; bottom-right panel: relation at $z = 9.5$.

Table 1: Parameters adopted in the Calculation Processes of the AGN LFs and AGN Number Counts

Parameter	Optical Band	X-ray Band
Eddington ratio	$\lambda = 0.25(M_{\text{BH}}/2 \times 10^9)^{0.5}$	$\lambda = 0.25(M_{\text{BH}}/2 \times 10^9)^{0.5}$
AGN lifetime (years)	2×10^7	9×10^7
α in $M_{\text{BH}} - \sigma$ relation (Robertson et al. 2006)	$8.01 - 0.138 \log(1 + z)$	$8.01 - 0.138 \log(1 + z)$
β in $M_{\text{BH}} - \sigma$ relation (Robertson et al. 2006)	4.02	4.02
α in $M_{\text{BH}} - \sigma$ relation (Gültekin et al. 2009)	8.12	8.12
β in $M_{\text{BH}} - \sigma$ relation (Gültekin et al. 2009)	4.24	4.24

Note. — The exception case is for the optical AGN LF at $z = 6$ given by Willott et al. (2010b): $\lambda = 2.0(M_{\text{BH}}/2 \times 10^9)^{0.5}$ and AGN lifetime of 2×10^5 yrs. α and β are defined as $\log(M_{\text{BH}}/M_{\odot}) = \alpha + \beta \log(\sigma/200 \text{ km s}^{-1})$.